Microchemical Journal 209 (2025) 112811

Contents lists available at ScienceDirect

Microchemical Journal

journal homepage: www.elsevier.com/locate/microc

Early diagnosis of Alzheimer's disease: Magnetic hexagonal boron nitride-based immunosensor platform for total tau detection☆

Simge Er Zeybekler [a,*,1], Dilek Odaci [b,2], Nesrin Horzum [a,*,3]

[a] Department of Engineering Science, Faculty of Engineering and Architecture, İzmir Katip Çelebi University, İzmir 35620 Turkey
[b] Department of Biochemistry, Faculty of Science, Ege University 35100 Bornova-Izmir, Turkey

ARTICLE INFO

Keywords:
Hexagonal boron nitride
Magnetic nanoparticles
T-Tau protein detection
Biofunctional surfaces
Nanobiotechnology
Immunosensing

ABSTRACT

Alzheimer's disease (AD) constitutes a complex pathological process and ranks among the leading causes of dementia globally. There is an escalating demand for diagnostic tools that are minimally invasive, timely, and accurate. The total Tau (T-Tau) protein in blood serum has emerged as a promising biomarker for the early diagnosis of AD. In this study, a magnetic hexagonal boron nitride (MHBN)-based immunosensor platform was developed to detect T-Tau in artificial blood serum. Following the exfoliation of hexagonal boron nitride (HBN), magnetite nanoparticles were deposited onto the surface of the HBN nanosheets, followed by (3-Aminopropyl) triethoxysilane (APTES) modification. The resulting MHBN-APTES nanocomposite-modified screen-printed carbon electrode acted as a matrix for immobilizing Anti-T-Tau antibodies. The analytical performance of the MHBN-APTES/Anti-T-Tau immunosensor in the presence of T-Tau isoforms was evaluated using cyclic voltammetry, differential pulse voltammetry, and electrochemical impedance spectroscopy techniques. The linear detection range was established at 0.5–50 pg/mL, with a limit of detection of 0.39 pg/mL for T-Tau, which is appropriate for identifying T-Tau in blood serum. The MHBN-APTES/Anti-T-Tau also demonstrated good repeatability, reproducibility, and stability, making it a dependable option for advanced applications.

1. Introduction

AD is a neurodegenerative disorder that leads to the loss of cognitive functions and is characterized by the presence of intracellular neurofibrillary tangles containing Tau protein [1,2]. T-Tau and phosphorylated Tau (P-Tau) levels are recognized as valuable biomarkers for the early detection of AD [3,4]. Cerebrospinal fluid (CSF) is frequently utilized as a physiological fluid for quantitative analysis of β-amyloid 42, T-Tau, P-Tau, and other biomarkers [5]. However, its use has several drawbacks, including invasiveness, time, cost, and limited accessibility in healthcare settings. While assessing AD biomarkers traditionally relies on CSF, plasma has been proposed as an optimal biofluid for detecting these biomarkers due to the absorption of approximately 500 mL of CSF into the blood daily [6]. Clinical investigations have demonstrated that the T-Tau protein levels in the blood plasma of individuals with AD are approximately two to three times higher than those in control subjects [7]. Nevertheless, the concentrations of the plasma biomarkers are notably lower, ranging from 10 to 100 times, compared to those in the CSF. Blood samples present challenges for accurate and reliable determination of blood-based biomarkers due to the presence of high levels of interfering substances. Traditional biomarker determination methods like enzyme-linked immunosorbent test, mass spectrometry, and surface plasmon resonance are time-consuming, require specialized personnel, and are costly. They also have complex procedures and limited sensitivity, making distinguishing between patients and healthy individuals difficult [8,9]. Simultaneously, incorporating multiple biological molecules into the medium escalates operational costs and presents challenges in maintaining system stability [10]. A precise and early diagnostic platform is essential for accurately detecting and quantitatively analysing blood-based biomarkers in the initial stages of AD.

Label-free electrochemical immunosensors are designed to directly ascertain the immune complex (antigen–antibody complex) by

☆ This article is part of a special issue entitled: 'PADs' published in Microchemical Journal.

* Corresponding authors.
E-mail addresses: simgeer89@gmail.com (S. Er Zeybekler), nesrin.horzum.polat@ikcu.edu.tr (N. Horzum).
[1] Orcid: 0000-0002-5814-0618.
[2] Orcid: 0000-0002-7954-1381.
[3] Orcid: 0000-0002-2782-0581.

https://doi.org/10.1016/j.microc.2025.112811
Received 25 November 2024; Received in revised form 5 January 2025; Accepted 17 January 2025
Available online 18 January 2025

quantifying the physical changes the complex formation brings. Consequently, these label-free electrochemical immunosensors present an extensive linear detection range, a low limit of detection (LOD), and swift measurements at a reduced cost due to their label-free detection and capacity for quantitative measurement [11]. Modifying electrode surfaces with diverse nanomaterials has enhanced the electrical conductivity, amplifying the detection sensitivity [12].

Two-dimensional hexagonal boron nitride (HBN), often referred to as white graphene, has seen a rise in utilization within electrochemical sensor applications due to its exceptional properties, including high chemical stability, a substantial specific surface area, a tunable band gap of approximately 5.5–6.0 eV, and rapid electron transport capability [13,14]. HBN nanomaterials can serve as effective fillers for producing high-performance polymer nanocomposites. By employing surface modifications with inorganic particles, it is possible to alter the surface characteristics of HBNs, including hydrophobicity, magnetic properties, and electrical properties. Magnetite nanoparticles (Fe_3O_4 NPs, MNPs), a semimetallic metal oxide with an cubic inverse spinel structure, exhibit outstanding adsorption capacity, high electrocatalytic properties, and inherent electrical conductivity [15,16]. The application of Fe_3O_4 NPs onto the electrode surface leads to an increase in electrode surface area, mass, electron transfer rate, selectivity, sensitivity, and, most significantly, an enhanced signal-to-noise ratio [17]. Furthermore, Fe_3O_4-based electrochemical sensors boast notable attributes, including cost-effectiveness, high sensitivity, and rapid response time [18]. The exclusive use of Fe_3O_4 NPs on the electrode surface is insufficient to achieve optimal surface area performance due to their natural tendency to aggregate. Consequently, their combination with nanomaterials such as graphene oxide and HBN yields a synergistic effect, enhancing their dispersion across the electrode surface [19].

In the present study, an immunosensor platform based on APTES-modified MHBN was developed for the detection of T-Tau protein in artificial blood serum. While graphene-based nanomaterials are commonly used as recognition surfaces for T-Tau detection [20–23], this study is the first to develope an MHBN-based recognition surface for this purpose. Moreover, the use of the APTES created a hydrophilic surface, enabling the successful immobilization of Anti-T-Tau, facilitated by amino groups on the surface. The working electrode of screen-printed carbon electrode (SPCE) was coated with MHBN-APTES nanocomposite using the drop-casting method, followed by the immobilization of Anti-T-Tau on the MHBN-APTES nanocomposite-modified SPCE using carbodiimide chemistry. Characterization of the MHBN-APTES nanocomposite at each modification stage was conducted using Scanning Electron Microscopy-Energy Dispersion X-ray Spectroscopy (SEM-

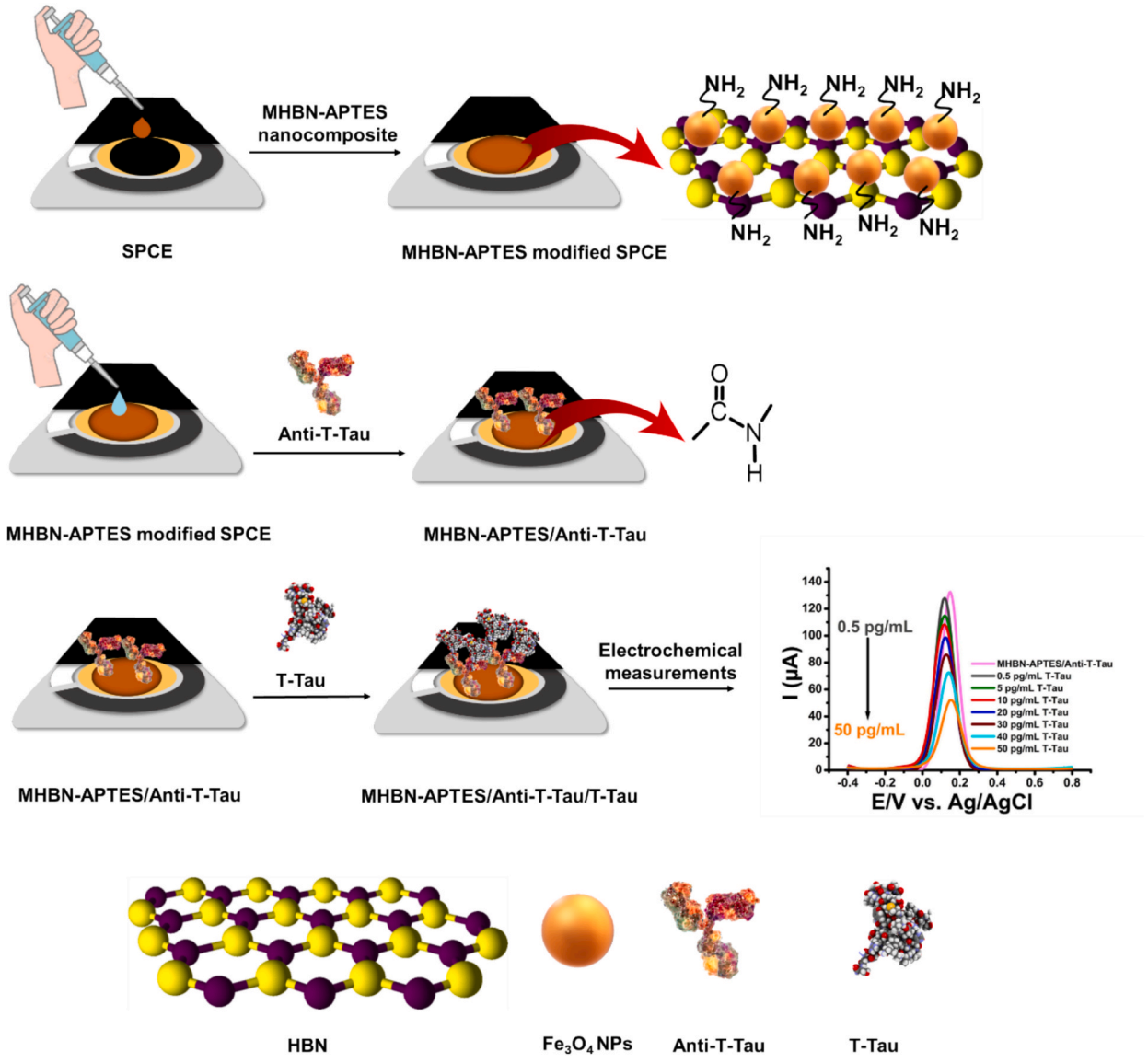

Scheme 1. Preparation steps for the MHBN-APTES/Anti-T-Tau nanocomposite and the electrochemical detection of T-Tau.

EDS), Attenuated Total Reflection–Fourier Transform Infrared Spectroscopy (ATR-FTIR), X-Ray Diffraction (XRD), and X-ray photoelectron spectroscopy (XPS). The electrochemical characterization of the developed MHBN-APTES/Anti-Tau immunosensor was evaluated using cyclic voltammetry (CV), differential pulse voltammetry (DPV), and electrochemical impedance spectroscopy (EIS) techniques in the presence of T-Tau. The study utilized a Tau protein ladder comprising six recombinant Tau proteins with molecular masses of 36.8, 39.7, 40.0, 42.6, 42.9, and 45.9 kDa, respectively, providing a combined amount of 0.25 μg for each of its six isoforms. The aim was to evaluate the T-Tau protein by analyzing the electrochemical current resulting from its interaction with the MHBN-APTES/Anti-T-Tau biofunctional surface rather than measuring each isoform separately. The MHBN-APTES/Anti-T-Tau/T-Tau immunosensor effectively detected T-Tau concentrations present in the blood serum of healthy individuals and its elevated levels in AD, demonstrating enhanced analytical performance. Scheme 1 illustrates the preparation steps for MHBN-APTES/Anti-T-Tau and the electrochemical detection of T-Tau.

2. Materials and method

2.1. Chemicals

Tau protein ladder, six isoforms (T7951), and Anti-T-Tau (SAB5500182) of rabbit monoclonal antibody were both purchased from Sigma-Aldrich (Germany). Boron nitride nanopowder (HBN) (790532, average particle size < 150 nm), $FeCl_3{\cdot}6H_2O$ (97 %), $FeCl_2{\cdot}4H_2O$ (99 %), ammonium hydroxide, 1-Methyl-2-pyrrolidone, (3-Aminopropyl)triethoxysilane (APTES), urea (99.0–100.5 %), bovine serum albumin (BSA, ≥98.0 %), insulin (INS), D-glucose (GLC, ≥99.5 %), potassium chloride, human serum (H4522), potassium hexacyanoferrate (III) (HCF, $K_3[Fe(CN)_6]$) were purchased from Sigma-Aldrich (Germany).

2.2. Apparatus

The HBN and MHBN-APTES nanocomposites were examined using XRD (Malvern Panalytical Empyrean, United Kingdom), XPS (Thermo Scientific K-Alpha, USA), ATR–FTIR (PerkinElmer Spectrum Two for a range of 4000–600 cm^{-1}, USA), and EDS (Thermo Scientific Apreo S, USA) techniques. The electrochemical measurements were performed using a PalmSens4 potentiostat (Palm Instruments Houten, Netherlands) in conjunction with a SPCE (C11L, 4 mm diameter), an Ag/AgCl reference electrode, and a carbon auxiliary electrode (Metrohm, Switzerland). The connection between the SPCE and the potentiostat was established using a 4 mm banana SPE Connector.

2.3. Synthesis of MHBN

0.5 g of commercial HBN powder were dispersed in 500 mL of 1-Methyl-2 pyrrolidone and then sonicated at 700 W for 6 h to obtain HBN nanosheets. After an overnight incubation, the white HBN nanosheets deposited on the solution's surface were precipitated by centrifugation at 14.000 rpm. The nanosheets underwent three washes with ethanol to eliminate the solvent, and the HBN layers were subsequently dried in an oven at 60 °C overnight [24].

To modify the HBN nanosheets with Fe_3O_4 NPs (MNPs), 100 mg of HBN was added to 100 mL of pure water and sonicated for 1 h. Subsequently, a 2:1 M ratio of Fe^{3+} to Fe^{2+} salts were added to the HBN solution while being stirred magnetically. The pH of the solution was adjusted to 8.0 at the onset of the reaction by gradually adding 3 mL of ammonium hydroxide. The reaction mixture was then magnetically stirred for 4 h under nitrogen (N_2) gas. Following the completion of the reaction, the synthesized MHBN nanocomposite was washed thrice with ultrapure water and subsequently dried at 65 °C [25,26].

2.4. Modification of MHBN nanocomposite with APTES

600 mg of MHBN was dispersed in 600 mL of ethanol and ultrapure water (5/1 ratio). The pH of the solution was adjusted to 4 using acetic acid, followed by 20 min of sonication. Subsequently, 4 mL of APTES was introduced into the solution, and the mixture was mechanically stirred at room temperature for 4 h. The resulting solution was centrifuged at 9000 rpm, and the MHBN-APTES nanocomposite was washed with ultrapure water and ethanol to eliminate any residual unreacted APTES. The obtained MHBN-APTES nanocomposite was then dried at 45 °C overnight and subjected to characterization [27].

2.5. Preparation of MHBN-APTES/Anti-T-Tau

The working electrode's surface underwent coating with MHBN-APTES nanocomposite utilizing the drop-casting technique. 4 μL of MHBN-APTES aqueous nanocomposite solution (4 mg/mL) was applied to the SPCEs' working electrode and dried for 30 min at room temperature. Before antibody immobilization, all electrodes were washed with DI water and dried. Following this, Anti-T-Tau immobilization was achieved using EDC/NHS carbodiimide chemistry on the MHBN-APTES nanocomposite-modified SPCEs. Stock Anti-T-Tau was prepared in the presence of 500 mM EDC, 20 mM NHS, and 1:100 Anti-T-Tau (approximately 0.25 μg/mL as a final concentration) in the 10 mM PBS (100 μL) and incubated at room temperature for 15 min. Then, 5 μL of this mixture was dropped onto the SPCE surface modified with the MHBN-APTES nanocomposite and incubated at room temperature for 2 h. As per the Anti-T-Tau usage datasheet provided by the manufacturer, diluting the stock Anti-T-Tau solution 100 times in PBS (0.01 M, pH 7.4) for immunohistochemistry is recommended. Before electrochemical measurements, all electrodes were washed with distilled water to remove unbound Anti-T-Tau.

2.6. Electrochemical measurements

All electrochemical measurements were performed using a SPCE connected to a PalmSens4 instrument (Palm Instruments Houten, Netherlands) and a computer running PSTrace 5.9 software. CV, DPV, and EIS measurements were conducted at room temperature (25.0 ± 0.5 °C). The CV and DPV measurements were carried out at a scan rate of 50 mV/s within the potential range of −0.4 to +0.8 V. For EIS, the frequency range was 0.21×10^{-4}–100 kHz, with an excitation voltage of 0.18 V and a DC potential of 10 mV. The measurements were performed in a 10 mM PBS (pH 7.4), containing 5.0 mM of HCF as the redox probe and 0.1 M KCl.

3. Results and discussion

3.1. Characterization of MHBN

The synthesized MHBN and MHBN-APTES nanocomposites were fully characterized using ATR-FTIR, SEM-EDS, and XPS. The ATR-FTIR spectrum of HBN (Fig. 1A) reveals a band at 1343 cm^{-1} correspoding to the out-of-plane bending vibrations of B—N—B bonds, while the band at 787 cm^{-1} representing the in-plane vibrations of B—N bonds.[26] After the modification with Fe_3O_4 NPs, a band in the range of 619–687 cm^{-1} appears,which is attributed to the symmetric stretching vibration of the Fe—O bond [28,29]. These observations align with existing literature, confirming the successful modification of HBN with Fe_3O_4 NPs. Following the modification of the MHBN nanocomposite with APTES, specific bands corresponding to the APTES are observed at 1100 cm^{-1} and 1017 cm^{-1}, indicating the presence of Si-O-Si bond vibrations. Additionally, the absorption band at 3464 cm^{-1} signifies the existence of free amine groups within the structure of the APTES [30,31].

The XRD pattern of HBN nanosheets displays seven distinct Bragg diffraction peaks, located at 2θ values of 26.6°, 41.7°, 43.9°, 50.1°,

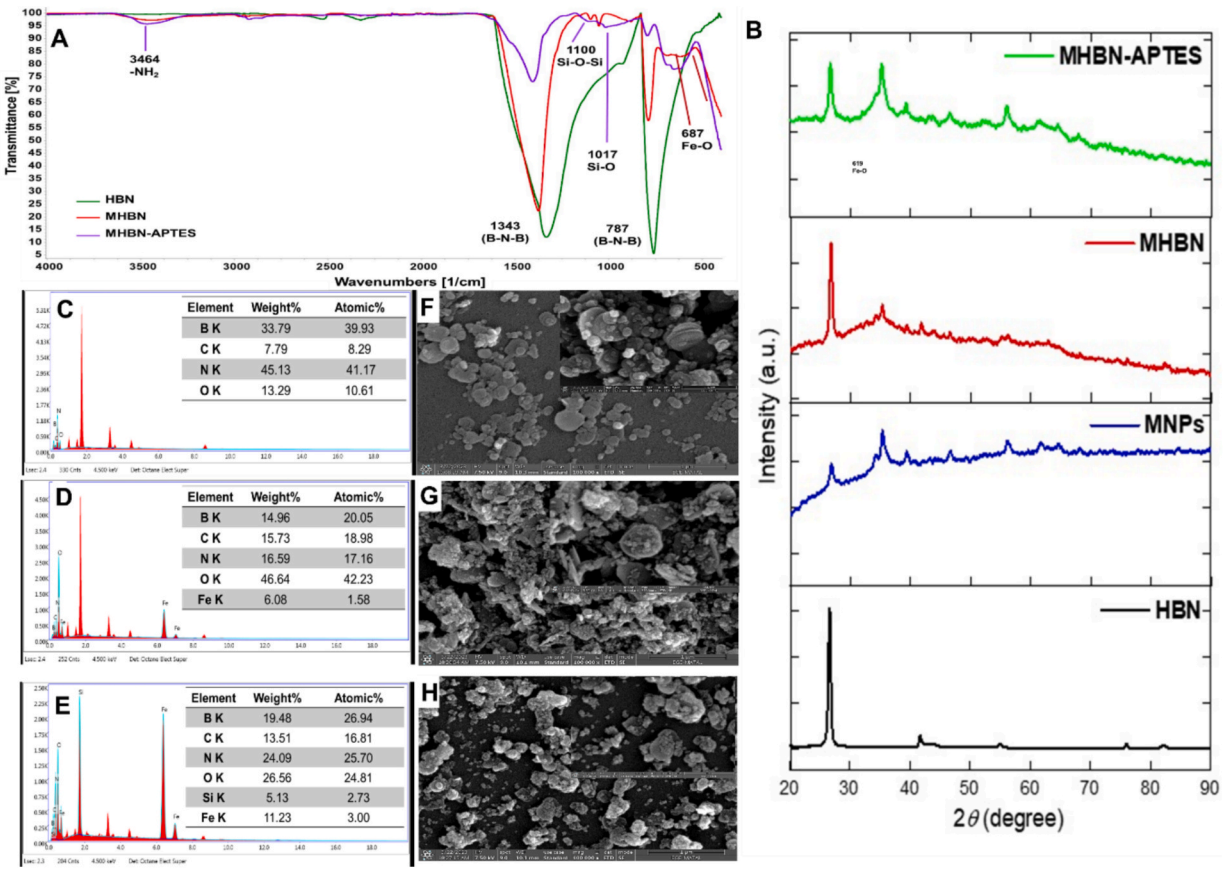

Fig. 1. A) ATR-FTIR spectrum of HBN, MHBN and MHBN-APTES nanocomposite, B) XRD patterns of HBN, MNPs, MHBN and MHBN-APTES, EDS spectra of C) HBN, D) MHBN, E) MHBN-APTES, SEM images (100.000× magnification, scale bar represents 1 μm) of F) exfoliated HBN, G) MHBN, H) MHBN-APTES nanocomposite (inset shows SEM images (250.000× magnification, scale bar represents 500 nm).

54.7°, 75.9°, and 82.1° (Fig. S1). These peaks correspond to the (0 0 2), (1 0 0), (1 0 1), (1 0 2), (0 0 4), (1 1 0), and (1 1 2) crystallographic planes, respectively. Notably, the intensity of the peaks associated with the (1 0 0), (1 0 1), (1 0 2), (0 0 4), (1 1 0), and (1 1 2) planes is considerably lower than that of the (0 0 2) plane. The detailed diffraction pattern of MHBN exhibits four additional peaks at 2θ values of 35.4°, 43.3°, 56.1°, and 61.8°, which correspond to the (3 1 1), (4 2 2), (5 1 1), and (4 4 0) planes, respectively [32]. These findings are in strong alignment with the cubic inverse spinel structure characteristic of magnetite nanoparticles (XRD pattern of MNPs in Fig. 1B) [33]. The Fe_3O_4 NPs that are deposited on the surface of HBN, referred to as MHBN, display distinct characterization peaks associated with the Fe_3O_4 lattice. This observation confirms the successful deposition of Fe_3O_4 NPs on the surface of HBN. Furthermore, the MHBN-APTES pattern reveals peaks similar to those observed in the MHBN pattern, indicating that the structural integrity of the material remains intact, even following surface modification.

The EDS data for HBN nanosheets, MHBN, and MHBN-APTES nanocomposites are presented in Fig. 1C–E. The EDS spectrum of the HBN nanosheets revealed the elemental composition percentages of boron (B), carbon (C), nitrogen (N), and oxygen (O) as 39.93 %, 8.29 %, 41.17 %, and 10.61 %, respectively. Following the modification of the HBN nanosheets with Fe_3O_4 nanoparticles, the elemental composition percentages of the resulting MHBN nanocomposite were determined to be 20.05 % for boron (B), 18.98 % for carbon (C), 17.16 % for nitrogen (N), 42.23 % for oxygen (O), and 1.58 % for iron (Fe). The EDS analysis confirmed the presence of iron in the nanocomposite's elemental composition. Furthermore, the increase in the atomic percentage of oxygen (from 10.61 % to 42.23 %) and the decrease in the atomic percentages of boron and nitrogen (from 39.93 % to 20.05 % and from 41.17 % to 17.16 %, respectively) support the conclusion of successful synthesis of Fe_3O_4 NPs on the surface of the HBN nanolayers. Following the modification of the MHBN nanocomposite with APTES, the peak intensities for boron (B), carbon (C), nitrogen (N), oxygen (O), silicon (Si), and iron (Fe) within the MHBN-APTES nanocomposite were analyzed. The resultant elemental composition percentages were determined to be 26.94 %, 16.81 %, 25.70 %, 24.81 %, 2.73 %, and 3.00 %, respectively. The presence of silicon confirms the successful modification of the MHBN nanocomposite with APTES.

Fig. 1F–H presents the SEM images of the synthesized MHBN-APTES nanocomposite at various magnifications obtained during each modification step. HBN nanolayers exhibited a uniform and well-distributed structure after the exfoliation process (Fig. 1F). Given that similar observations have been reported in existing literature, it can be concluded that the exfoliation of HBN was executed successfully [34–37]. Following the modification of HBN nanosheets with Fe_3O_4 NPs and APTES, the presence of iron nanoparticles on the surface of the nanosheets is clearly observed in Fig. 1G–H. The images obtained are also consistent with findings reported in the existing literature [37,38].

To gain deeper insights into the surface chemistry and bonding interactions, the synthesized MHBN-APTES nanocomposite was further analyzed using XPS characterization (Fig. 2). The XPS survey spectrum for HBN, along with HBN and HBN-APTES nanocomposites, is illustrated in Fig. 2A. The emergence of the Fe 2p peak in the XPS survey spectrum following the modification of HBN with Fe_3O_4 NPs provides clear evidence of the deposition of Fe_3O_4 NPs onto the surface of the HBN nanolayers. Furthermore, detecting the Si 2p peak after the modification of the MHBN nanocomposite with APTES confirms the efficacy of the APTES modification process. Upon examining the data presented in Fig. 2B, which compares weight percentage values derived from XPS

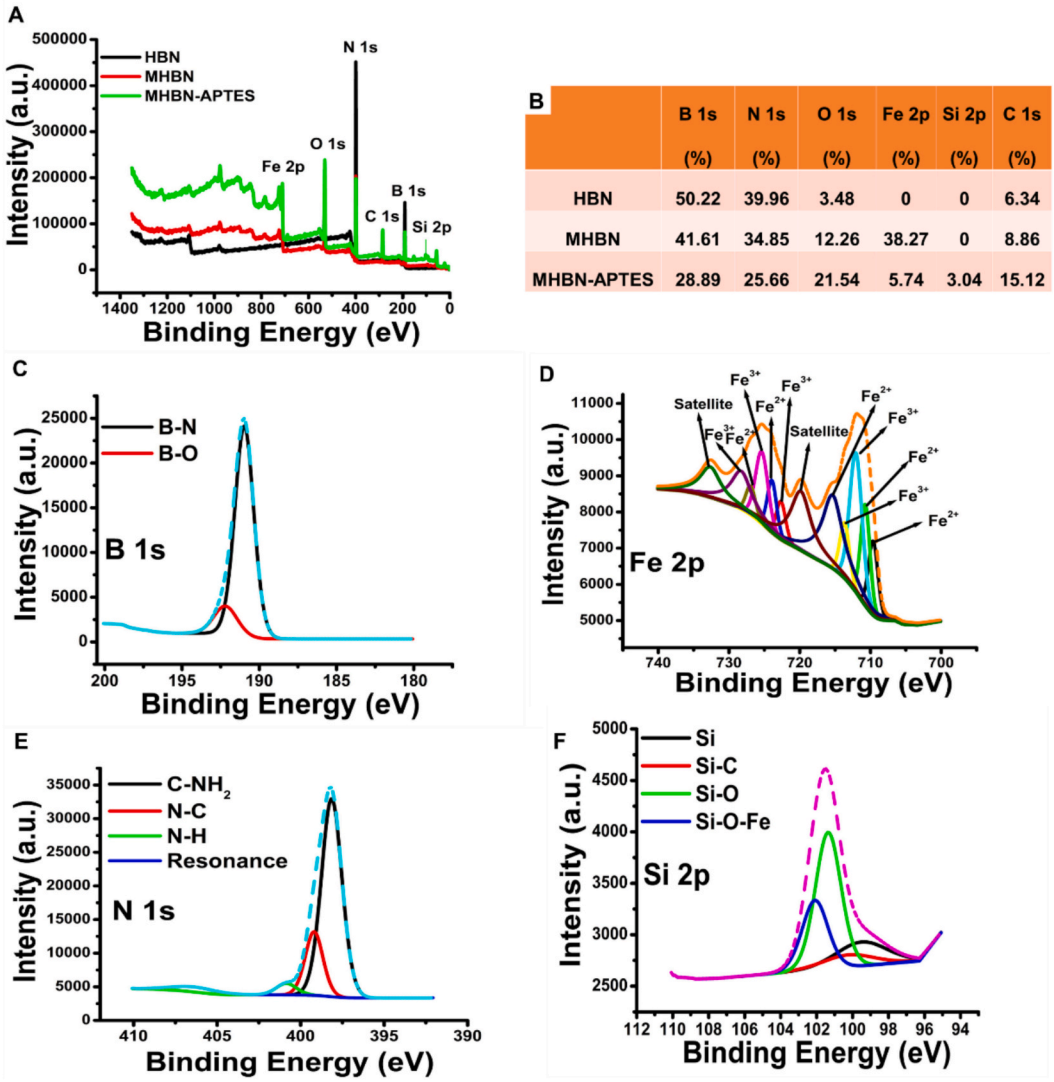

	B 1s (%)	N 1s (%)	O 1s (%)	Fe 2p (%)	Si 2p (%)	C 1s (%)
HBN	50.22	39.96	3.48	0	0	6.34
MHBN	41.61	34.85	12.26	38.27	0	8.86
MHBN-APTES	28.89	25.66	21.54	5.74	3.04	15.12

Fig. 2. A) XPS survey spectra and, B) chemical composition of HBN, MHBN, and MHBN-APTES, along with high-resolution XPS spectra of C) B 1s, D) Fe 2p, E) N 1s, and F) Si 2p of MHBN-APTES.

analysis, similar to the results obtained from EDS, the detection of iron on the surface of the HBN nanocomposite following the modification of HBN nanosheets with Fe_3O_4 NPs is detected. Additionally, there is a significant increase in the atomic percentage of oxygen, which rises from 3.48 % to 12.26 %. Concurrently, there is a reduction in the atomic percentages of B and N, decreasing from 50.22 % to 41.61 % and from 39.96 % to 34.85 %, respectively. These changes are strong indicators of the synthesis of Fe_3O_4 nanoparticles on the surface of HBN nanolayers. The increase in the carbon ratio, from 6.34 % to 15.52 % following the modification with APTES, can be attributed to the presence of the carbon chain in the APTES structure. Conversely, the notable reduction in the iron ratio, from 38.27 % to 5.74 % in the MHBN nanocomposite after APTES modification, further confirms the efficacy of the surface modification process. Additionally, the close alignment of the elemental percentages for N and Si obtained from the EDS analysis (25.70 % and 2.73 %, respectively) with those derived from the XPS analysis (25.66 % and 3.04 %, respectively) serves as evidence of the correlation between these methods. The B 1s XPS spectrum analysis indicates that the peak associated with the B–N bond is positioned at 190.3 eV. The peak corresponding to the formation of B–O bonds is observed at approximately 192.0 eV, as illustrated in Fig. 2C [39–41]. The Fe 2p spectrum acquired following the modification of HBN nanosheets with Fe_3O_4 nanoparticles reveals peaks at 728.2 eV ($2p_{1/2}$), 725.3 eV ($2p_{1/2}$), 722.6 eV ($2p_{1/2}$), 713.6 eV ($2p_{3/2}$), 712.0 eV ($2p_{3/2}$), which are indicative of the presence of Fe^{3+} species. Additionally, the spectrum exhibits other peaks at binding energies of 726.9 eV ($2p_{1/2}$), 723.9 eV ($2p_{1/2}$), 715.3 eV ($2p_{3/2}$) 709.6 eV ($2p_{3/2}$), 710.7 eV ($2p_{3/2}$), signifying the presence of Fe^{2+} species (Fig. 2D) [42,43]. The observed peaks at 719.8 eV and 732.6 eV were satellite peaks, indicating the high purity and synthesis of Fe_3O_4 NPs on HBN nanosheets. Specifically, the concurrent presence of Fe $2p_{1/2}$ (725.3 eV) and Fe $2p_{3/2}$ (710.7 eV) aligns closely with the standard data for Fe_3O_4 NPs [43–48]. In the N 1s spectrum (Fig. 2E), the peak observed at 400.9 eV post-silanization signifies the presence of N associated with N–H bonds originating from APTES. The prominent peak at 398.1 eV is attributed to C–NH_2 bonds, while the peak located at 399.2 eV corresponds to N–C bonds. The peak observed at 406 eV can be linked to the π^* resonances of the HBN crystal, indicating the existence of different bonding environments [49–52]. In the Si 2p spectrum of MHBN-APTES nanocomposite, it was observed that the peak at 100.2 eV corresponds to Si-C bonds, while the peak at 101.4 eV is associated with Si-O bonds, which are characteristic of APTES interactions. Additionally, the peak at 102.1 eV is attributed to the Si-O-Fe bond (APTES grafting Fe_3O_4). The peak located at 99.5 eV is assigned to elemental Si (Fig. 2F) [49,53–58].

3.2. Electrochemical characterization

The CV and DPV measurements were conducted utilizing HBN to assess the impact of each component within the MHBN-APTES nanocomposite on the current response (Fig. 3A–B). The bare SPCE displays quasi-reversible redox peaks, showing a peak-to-peak separation or potential difference (ΔE_p) of 0.24 V. The ΔE value of HBN-modified SPCE increased to 0.34, while the current value decreased compared to the bare SPCEs. This observation can be attributed to the semiconductor properties inherent in the HBN nanocomposite [59]. Moreover, electrochemical measurements were performed at concentrations of 1, 2, 4, and 5 mg/mL to optimize the MHBN-APTES nanocomposite concentrations on the working electrode of the SPCE. The modified SPCE using MHBN-APTES at concentrations of 1, 2, 4, and 5 mg/mL demonstrated a superior current response compared to the HBN-modified SPCE. The calculated ΔE_p values for the respective concentrations were 0.14, 0.13, 0.11, and 0.12 V. This observation indicates that the electron transfer rate at the MHBN-APTES-modified SPCE is better than that at the HBN-modified SPCE. MNPs on the HBN nanolayers enhance electron transfer efficiency through a synergistic effect between HBN and MNPs [19,60–63]. Moreover, the redox reaction is classified as quasi-reversible when the anodic and cathodic peak potential separation values (ΔE_p) exceed 59 mV [64]. Based on the obtained ΔE_p results, the redox reaction occurring on the electrode surface is quasi-reversible. Additionally, the graph in Fig. 4 supports this result. An increase in current was observed in both DPV and CV profiles with the increasing MHBN-APTES nanocomposite concentration. The observed increase in redox current can be attributed to several factors, including the substantial surface area of MNPs, high electron transfer capacity, and a pronounced synergistic effect with HBN. Additionally, the pKa value of the amine groups in APTES is 10.8 [65,66]. Consequently, the amine groups on the surface of the MHBN-APTES nanocomposite acquire a positive charge in PBS at pH 7.4. This results in electrostatic attraction with the anionic HCF solution, enhancing the current response. The responses obtained with the 5 mg/mL and 4 mg/mL MHBN-APTES nanocomposites were almost identical, which can be attributed to creating the steric hindrance by MHBN-APTES nanocomposite. Consequently, the optimal concentration of the MHBN-APTES nanocomposite was determined to be 4 mg/mL.

To establish the optimal duration for the immobilization of Anti-T-Tau on the MHBN-APTES modified SPCE surface, DPV measurements were conducted using a constant T-Tau concentration of 10 pg/mL at 1, 2, and 24-hour intervals. For the measurements undertaken after 24 h, the MHBN-APTES/Anti-T-Tau electrodes were initially maintained at room temperature for 2 h and subsequently stored in a refrigerator at 4 °C in a petri dish until the following day when the measurements were executed. After dropping 4 μL of a 10 pg/mL T-Tau solution to the prepared MHBN-APTES/Anti-T-Tau immunosensors for each specified period, the electrodes were incubated for 30 min at room temperature and washed with PBS. The results from the DPV measurements indicated that extending the immobilization time of Anti-T-Tau from 1 h to 2 h yielded an increased current difference when interacting with the 10 pg/mL T-Tau solution. However, at the end of the 24 h, the current response observed in the DPV measurements with 10 pg/mL T-Tau was nearly identical to the current difference recorded at the 2-hour, likely due to the steric hindrance caused by MHBN-APTES/Anti-T-Tau (Fig. 3C–D). Based on the DPV profile, the optimal time for immobilizing Anti-T-Tau on the MHBN-APTES-modified SPCE surface was determined to be 2 h.

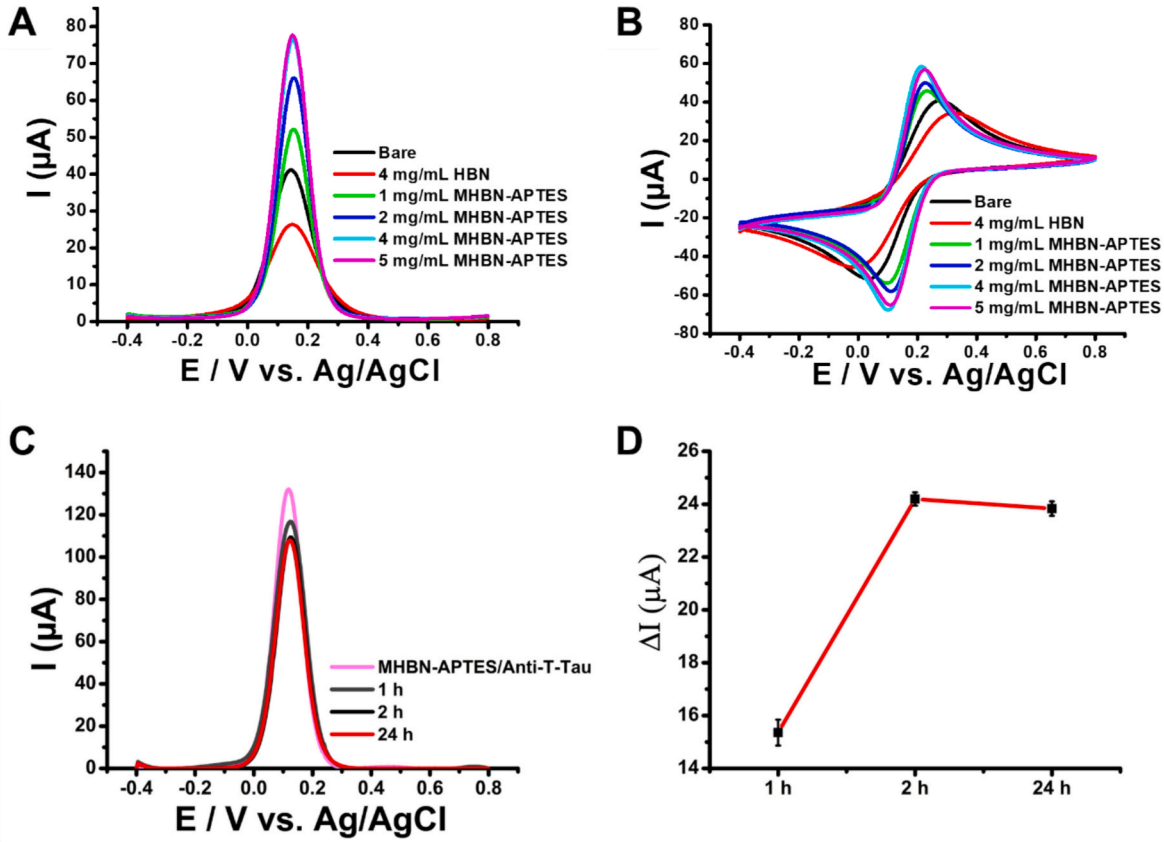

Fig. 3. A) DPV profiles of bare SPCE, SPCE/HBN (4 mg/mL), SPCE/MHBN-APTES (various concentrations), B) CV profiles of bare SPCE, SPCE/HBN (4 mg/mL), SPCE/MHBN-APTES (various concentrations), C) DPV profile obtained with MHBN-APTES/Anti-T-Tau electrodes at the end of 1, 2 and 24 h in the presence of 10 pg/mL T-Tau, D) Current difference graph corresponding to DPV measurements performed with MHBN-APTES/Anti-T-Tau electrodes at the end of 1, 2 and 24 h (All measurements were conducted in 10 mM PBS at pH 7.4, supplemented with 5.0 mM HCF and 0.1 M KCl. The scan rate employed for the analysis was 50 mV/s, c(T-Tau) = 10 pg/mL, error bars show the SD of 3 replicate measurements).

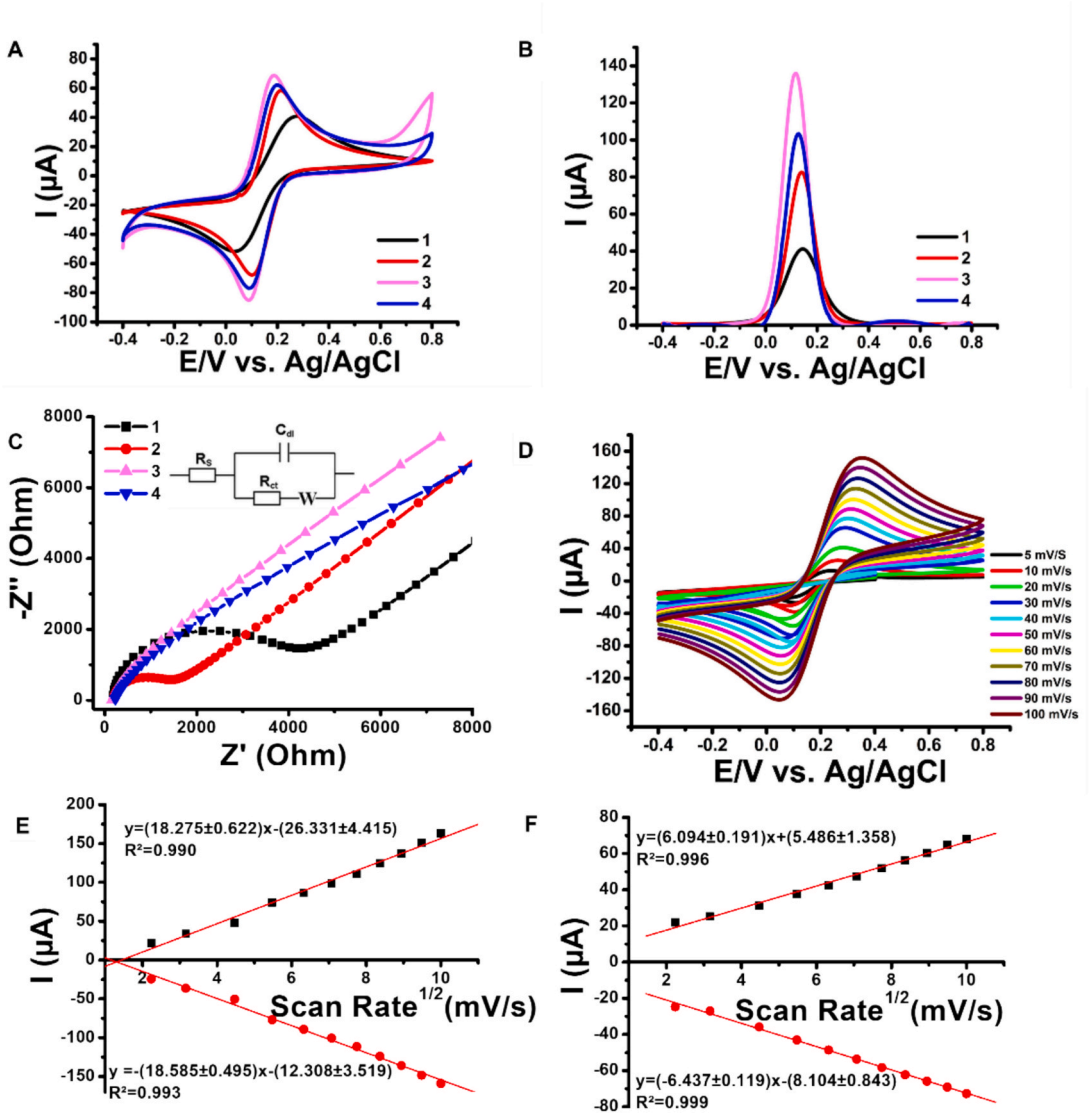

Fig. 4. A) CV profile, bare SPCE (1), MHBN-APTES (2), MHBN-APTES/Anti-T-Tau (3), MHBN-APTES/Anti-T-Tau /T-Tau (4), B) DPV profile, bare SPCE (1), MHBN-APTES (2), MHBN-APTES/Anti-T-Tau (3), MHBN-APTES/Anti-T-Tau/T-Tau (4), C) Nyquist profile, bare SPCE (1), MHBN-APTES (2), MHBN-APTES/Anti-T-Tau (3), MHBN-APTES/Anti-T-Tau/T-Tau (4), D) CV profile of MHBN-APTES modified SPCE at different scan rates (5–100 mV/s), E) graph shows the correlation between the peak currents obtained with the square root of the scan rates with MHBN-APTES surface, the equations were calculated as y = (18.275 ± 0.622)x − (26.331 ± 4.415) (R^2 = 0.990) and y = −(18.585 ± 0.495)x − (12.308 ± 3.519) (R^2 = 0.993), for I_{anodic} and $I_{catodic}$ respectively, F) graph, square root of scan rate and peak obtained with bare electrode surface, the equations were calculated as y = (6.094 ± 0.191)x + (5.486 ± 1.358) (R^2 = 0.996) and y = (−6.437 ± 0.119)x − (8.104 ± 0.843) (R^2 = 0.993) for I_{anodic} and $I_{catodic}$, respectively, (All measurements were conducted in 10 mM PBS at pH 7.4, supplemented with 5.0 mM HCF and 0.1 M KCl. The scan rate employed for the analysis was 50 mV/s, c(T-Tau) = 20 pg/mL).

The electrochemical characterization of bare, MHBN-APTES, MHBN-APTES/Anti-T-Tau and MHBN-APTES-APTES/Anti-T-Tau/T-Tau SPCE surfaces was conducted utilizing CV, DPV, and EIS measurements. The electrochemical oxidation and reduction peaks of HCF were evident in the CV profiles for all tested electrodes (Fig. 4A). The CV profiles indicated the mean anodic current values of 48.7 ± 0.8 μA, 58.8 ± 1.9 μA, 68.6 ± 0.5 μA, and 62.7 ± 1.7 μA for the bare, MHBN-APTES, MHBN-APTES/Anti-T-Tau, and MHBN-APTES/Anti-T-Tau/T-Tau modified SPCEs, respectively. Also, the calculated ΔE_p values for the bare, MHBN-APTES, MHBN-APTES/Anti-T-Tau, and MHBN-APTES/Anti-T-Tau/T-Tau modified SPCEs were 0.24, 0.12, 0.09, and 0.11, respectively. Following the modification of the bare SPCE with the MHBN-APTES nanocomposite, an increase in current was observed. As explained above in the section on determining the optimum nanocomposite concentration, this enhancement can be attributed to the protonation of the amine groups (pKa value 10.8) of APTES in PBS (pH 7.4), resulting in electrostatic attraction with the anionic HCF solution, which consequently increased the current response [65,66]. The observed increase in redox current can also be ascribed to the high surface area of MNPs, their high electron transfer capacity, and the pronounced synergistic effect with HBN [19,60]. Likewise, the MHBN-APTES/Anti-T-Tau electrodes exhibited improved peak current and decreased ΔE_p value compared to the MHBN-APTES, indicating enhanced conductivity and electrochemical reactivity [63]. As antibodies exist as polyelectrolytes in aqueous solutions, their electric charges can be influenced by the pH of the buffer utilized during electrochemical measurements and the immobilization process. Typically, the isoelectric point of the $(F_{ab})_2$ regions of antibodies exceeds that of the F_c fragment and the entire antibody [67,68]. Consequently, under buffer conditions, $(F_{ab})_2$ fragments possess a positive charge, while the F_c fragment exhibits a negative charge [69,70]. The positive charge of $(F_{ab})_2$ fragments leads to electrostatic attraction with the anionic redox solution of HCF, which

enhances the electron transfer rate. All these can be considered as a reason for the signal increase obtained after binding of Anti-T-Tau to the MHBN-APTES surface. In electrochemical measurements conducted in the presence of T-Tau, a decrease in current and ΔE_p value was recorded due to the redox-active species' inability to access the electrode surface. This results from forming an immunocomplex between Anti-T-Tau and T-Tau on the electrode surface.

Following CV, DPV is employed for quantitatively detecting analytes owing to its low detection limits, diminished capacitive current, and reduced background noise characteristics. The current is measured both before and following the application of the pulse, with the difference calculated to mitigate the contribution of capacitive current in the overall measurement, thereby enhancing selectivity [67,71]. This technique facilitates peak separation even within narrow wavelength ranges, making it particularly suitable for this study's quantitative detection of T-Tau. Fig. 4B illustrates the DPV profiles of bare, MHBN-APTES, MHBN-APTES/Anti-T-Tau, and MHBN-APTES/Anti-T-Tau/T-Tau modified SPCEs. Consistent with the CV profiles, a notable increase in current was observed after the SPCE surface was coated with the MHBN-APTES nanocomposite and the Anti-T-Tau was immobilized. Conversely, a decrease in current was recorded during electrochemical measurements conducted in the presence of T-Tau. In this regard, it was confirmed that all DPV profiles align with the trends indicated in the CV profiles.

EIS was also performed to investigate ion-charge transfer resistance (R_{ct}) and electrochemical properties of the modified SPCEs. This approach quantifies the current response by applying a sinusoidal voltage. When impedance spectra are depicted as a Nyquist plot, the linear segment at lower frequencies, characterized by a 45° angle, indicates a diffusion-limited process. Conversely, the semicircular segment at higher frequencies illustrates the R_{ct} and double-layer capacitance [72,73]. The diameter of the semicircle formed in the Nyquist plot is inversely proportional to electrical conductivity, allowing for the assessment of variations in R_{ct} at each modification stage based on this semicircular diameter. Moreover, the linear trend observed at low frequencies within the Nyquist plot signifies rapid electron transfer [19]. The insulating layer formed by the antibody-antigen immunocomplex on the electrode surface inhibits the diffusion of redox-active molecules to the electrode. This results in a change in capacitance, which leads to an increased R_{ct} in the EIS profile of the electrodes. Randles equivalent circuit model (R_s: solution resistance, R_{ct}: ion-charge transfer resistance, W: Warburg element, and C_{dl}: double-layer capacitance) was used for fitting based on the experimental data. All fitting parameters and the chi-squared (χ^2) values (with estimated errors) were provided in Table S1. According to this circuit model, the mean R_{ct} values for the bare, MHBN-APTES, MHBN-APTES/Anti-T-Tau, and MHBN-APTES/Anti-T-Tau/T-Tau modified SPCE were calculated at 3338 ± 178.5 Ω, 1125 ± 29.7 Ω, 25.1 ± 5.4 Ω, and 55.5 ± 6.5 Ω, respectively. A notable decrease in R_{ct} was observed in the Nyquist profile following the modification of the bare SPCE with the MHBN-APTES nanocomposite and subsequent covalent attachment of Anti-T-Tau to the surface of the MHBN-APTES nanocomposite-modified SPCE. This phenomenon, similar to that indicated by the CV profile, suggests an increase in surface area due to the MHBN-APTES modification, thereby facilitating electron transport between ferri/ferrocyanide ($[Fe(CN)_6]^{3-/4-}$) ions [74]. Upon the incubation of the MHBN-APTES/Anti-T-Tau surface with T-Tau, the formation of an immunocomplex between the MHBN-APTES/Anti-T-Tau surface and T-Tau impedes electron transfer between the redox probe (HCF) and the electrode surface, resulting in an observed increase in R_{ct} (Fig. 4C). These findings indicate that the Nyquist profiles align with the results obtained from the CV and DPV profiles [75–78].

The scan rate serves as a crucial parameter for controlling the applied potential. The MHBN-APTES surface was analyzed at varying scan rates (0–100 mV/s) to investigate the correlation between the scan rate and its current values (Fig. 4D). As illustrated in Fig. 4D, an increase in the scan rate resulted in a shift of the anodic peak to a higher potential value. In comparison, the cathodic peaks shifted to a lower potential value. The rising ΔEp value as a function of increasing scan rate suggest that the electron transfer kinetics are quasi-reversible. Additionally, the linear relationship observed with the square root of the anodic and cathodic current scan rate peaks indicates that the redox reaction is governed by diffusion-controlled behavior [79]. The equations were calculated as y=(18.275 ± 0.622)x-(26.331 ± 4.415) ($R^2 = 0.990$) and y =-(18.585 ± 0.495)x-(12.308 ± 3.519) ($R^2 = 0.993$), respectively. From these findings, it can be concluded that the MHBN-APTES surface exhibits diffusion-controlled behavior at varying scan rate. Applying the Randles-Sevcik equation (1), from the slope of the plot ($I_p = f(v^{1/2})$) the electroactive surface area for the bare SPCE and MHBN-APTES electrodes were determined to be 0.059 cm^2 and 0.124 cm^2, respectively.

$$I_p = (2.69 \times 10^5) n^{3/2} D^{1/2} C A v^{1/2} \quad (1)$$

I_p = peak current (Ampere).
n = number of e-involved (equal to 1).
D = diffusion coefficient (for $K_3[Fe(CN)_6]$ is 7.6×10^{-6} cm^2/s),
A = electroactive surface area (cm^2),
C = concentration of $K_3[Fe(CN)_6]$ (mol/cm^3),
v = scan rate (V/s).

The electro active surface area of bare SPCE and MHBN-APTES modified SPCE was determined from the peak current plots corresponding to the bare electrode surface as a function of the square root of scan rates, as depicted in Fig. 4E-F. Upon modification of the bare SPCE with MHBN-APTES, there was an approximately two-fold increase in the electroactive surface area compared to that of the bare SPCE. This enhancement suggests that the MHBN-APTES nanocomposite $Fe(CN)_6^{3-/4-}$ facilitates additional conduction pathways for electron transfer [19].

3.3. Application of MHBN-APTES/Anti-T-Tau for the detection of t-tau

To ascertain the linear detection range of T-Tau utilizing the MHBN-APTES/Anti-T-Tau immunosensor, DPV measurements were conducted across varying concentrations of T-Tau, ranging from 0.5 to 100 pg/mL. The linear detection range was from 0.5 to 50 pg/mL. The calibration curve equation was calculated as y = (1.336 ± 0.051)x + (7.515 ± 1.445) ($R^2 = 0.993$), where x represents the T-Tau concentration in pg/mL, and y represents the current in μA (Fig. 5A-B). The interaction between Anti-T-Tau and T-Tau on the electrode surface resulted in an immunocomplex, as evidenced by the DPV measurements conducted within the 0.5 to 50 pg/mL concentration range. This interaction impeded the access of HCF to the electrode surface, leading to a reduction in current as T-Tau concentration increased. Notably, no significant increase in current density was observed beyond the T-Tau concentration of 50 pg/mL. This phenomenon can be attributed to the steric hindrance caused by T-Tau on the electrode surface. Furthermore, the DPV profile corresponding to the incremental T-Tau concentrations from 0.5 to 50 pg/mL was presented in Fig. 5C. The plasma T-Tau levels in healthy individuals are reported at 3.07 pg/mL [80]. In patients with mild cognitive impairment, this value rises to 4.6 pg/mL [81]. Furthermore, individuals diagnosed with AD exhibit a significantly elevated T-Tau concentration of 37.5 pg/mL [7]. The linear detection range of the developed MHBN-APTES/Anti-T-Tau immunosensor is well-suited for T-Tau detection in blood plasma.

The LOD denotes the minimum quantity of an analyte that can be identified with a specified degree of confidence [82]. In this study, DPV measurements were employed to ascertain the LOD of the MHBN-APTES/Anti-T-Tau immunosensor, utilizing a total of 10 distinct immunosensors. The lowest concentration point on the calibration graph, 0.5 pg/mL of T-Tau, was used for the LOD calculation. The formula applied for determining the LOD was 3SD/m, where SD represents the standard deviation of 10 measurements conducted at the 0.5 pg/mL T-Tau concentration, and m signifies the slope of the T-Tau calibration

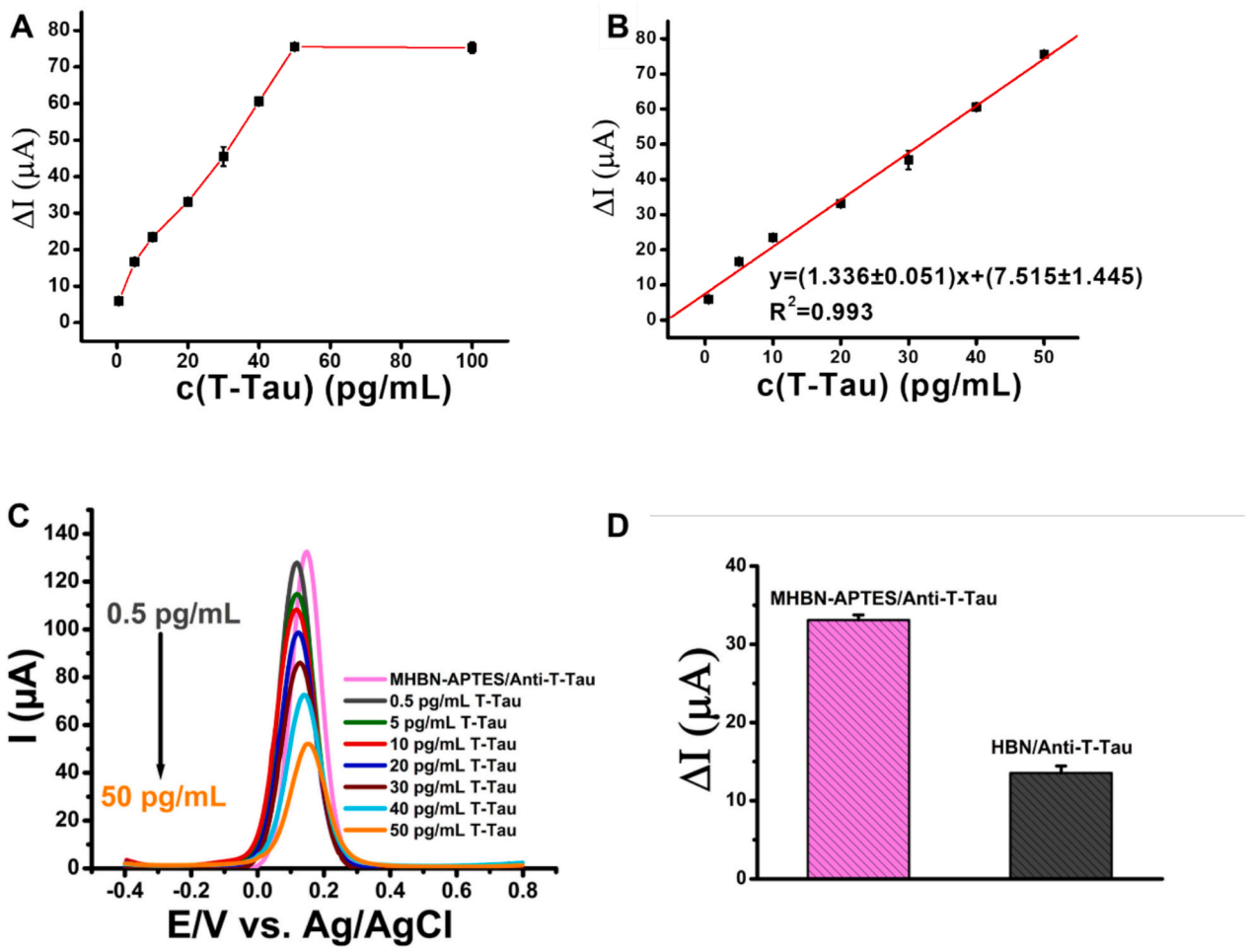

Fig. 5. A) Effect of T-Tau concentration on the current response, B) Linear detection range for T-Tau detection by MHBN-APTES/Anti-T-Tau modified SPCE, C) DPV profile corresponding to increasing T-Tau concentration between 0.5 and 50 pg/mL, D) Effect of each component on the immunosensor response, (All measurements were conducted in 10 mM PBS at pH 7.4, supplemented with 5.0 mM HCF and 0.1 M KCl. The scan rate employed for the analysis was 50 mV/s, c(T-Tau) = 20 pg/mL, error bars show the SD of 3 replicate measurements).

curve [83]. Consequently, the calculated LOD for T-Tau was determined to be 0.39 pg/mL.

HBN/Anti-T-Tau modified SPCEs were prepared, and the impact of each component on the sensor response was evaluated utilizing the DPV technique in the presence of 20 pg/mL T-Tau (Fig. 5D). It was observed that the DPV measurements conducted with HBN/Anti-T-Tau demonstrated significantly inferior performance compared to the MHBN-APTES/Anti-T-Tau surface. Govind Rajan et al. (2019) noted that the contact angle of the HBN basal plane was measured at 81°, indicating low hydrophilicity [84]. It is well-established that surface hydrophilicity plays a critical role in the effective immobilization of biological molecules [85]. Consequently, the lower immobilization efficiency of Anti-T-Tau on the HBN nanosheets can be attributed to this characteristic. The coating of the electrode surface with MHBN-APTES to the electrode surface enhances hydrophilicity due to the presence of amine functional groups derived from APTES. Consequently, a greater quantity of Anti-T-Tau was effectively immobilized on the surface of the SPCE modified with MHBN-APTES. Literature supports the notion that the incorporation of Fe_3O_4 NPs into nanomaterials such as graphene or HBN leads to synergistic effects that enhance the activity of Fe_3O_4 and increase the available surface area [19,86]. Therefore, the synergistic interaction between HBN and Fe_3O_4 NPs, along with the surface hydrophilicity induced by the presence of amine groups on the electrode surface, demonstrated superior performance for the detection of T-Tau compared to the HBN-modified SPCE surface.

The selectivity of an analytical method is defined by its capability to detect the analyte while remaining unaffected by other components within the matrix. In this context, BSA, GLC, INS, and urea have been identified as potential interfering substances in the blood that may influence the MHBN-APTES/Anti-T-Tau immunosensor response. Reference range for BSA [87], GLC [88], INS [89], and urea [90,91] were established based on existing literature. The selectivity of the MHBN-APTES/Anti-T-Tau immunosensor was assessed through DPV measurements, employing 20 pg/mL T-Tau solutions that included 4.0 g/dL BSA, 100 mg/dL GLC, 10 μU/mL INS, and 14 mg/dL urea. The findings indicated that the selectivity of the immunosensor was 98.48 % for the combination of T-Tau and BSA, 96.65 % for T-Tau and GLC, 97.51 % for T-Tau and urea, and 97.20 % for T-Tau and INS. Additional selectivity studies were conducted for each molecule alone, yielding values of 1.63 % for BSA, 2.84 % for GLC, 2.79 % for urea, and 0.99 % for INS (Fig. 6A-B). Based on the obtained data, it can be concluded that BSA, GLC, INS, and urea, individually or in conjunction with T-Tau, do not interfere with the developed MHBN-APTES/Anti-T-Tau immunosensor response.

3.4. Repeatability, reproducibility, and stability of MHBN-APTES/Anti-T-Tau immunosensor

Repeatability studies were conducted in the presence of 20 pg/mL T-Tau by performing ten measurements on a single electrode (Fig. 7A). The resulting coefficient of variation (%cv) and SD values were 2.47 %

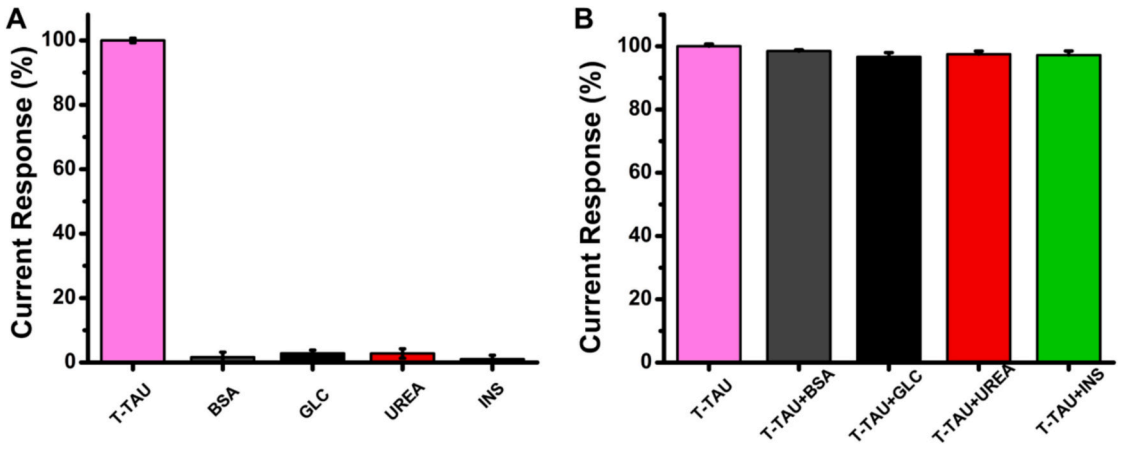

Fig. 6. A) Interference effect of BSA, GLC, UREA and INS on the MHBN-APTES/Anti-T-Tau immunosensor response alone, B) Interference effect of BSA, GLC, UREA and INS on the determination of T-Tau by MHBN-APTES/Anti-T-Tau immunosensor. (c(T-Tau) = 20 pg/mL, [BSA] = 4.0 g/dL, [GLC] = 100 mg/dL, [Urea] = 14 mg/dL, [INS] = 10 μU/mL) (All measurements were conducted in 10 mM PBS at pH 7.4, supplemented with 5.0 mM HCF and 0.1 M KCl. The scan rate employed for the analysis was 50 mV/s, error bars show the SD of 3 replicate measurements).

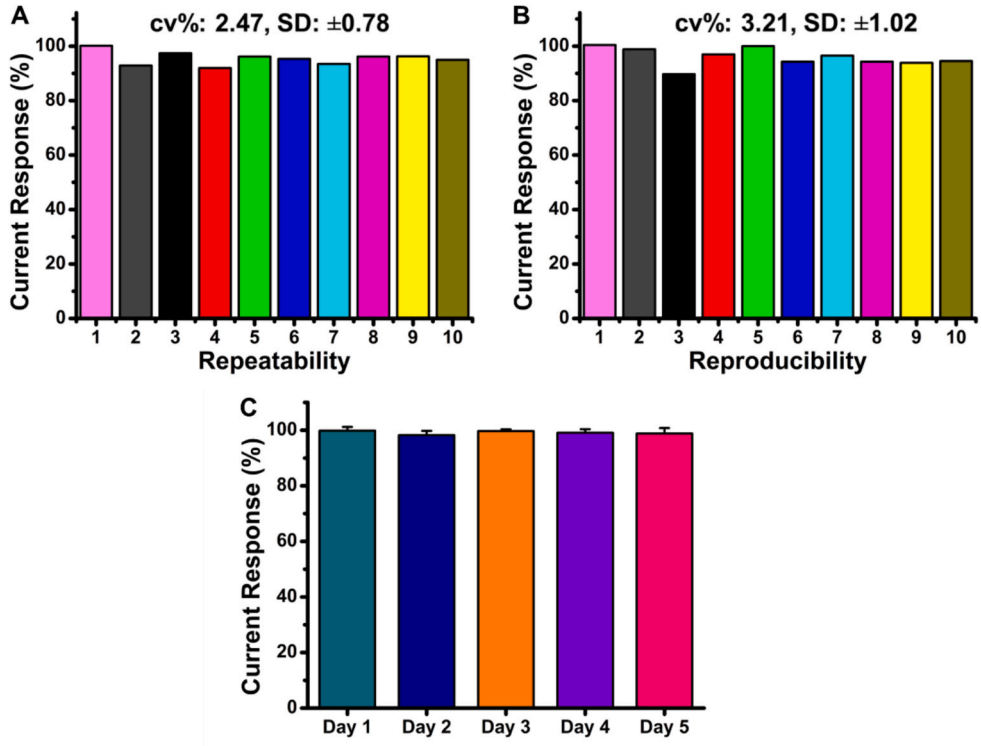

Fig. 7. A) Assessment of repeatability, indicated by the current response (%) from ten repeated measurements conducted on a single MHBN-APTES/Anti-T-Tau immunosensor, B) Evaluation of reproducibility, demonstrated by the current response from a single measurement taken on ten distinct MHBN-APTES/Anti-T-Tau immunosensors that were prepared independently. C) Stability study, wherein MHBN/Anti-T-Tau immunosensors were examined over a five-day storage period at a temperature of 4 °C. (All measurements were conducted in 10 mM PBS at pH 7.4, supplemented with 5.0 mM HCF and 0.1 M KCl. The scan rate employed for the analysis was 50 mV/s, c(T-Tau) = 20 pg/mL, error bars show the SD of 3 replicate measurements).

and ± 0.78, respectively. These findings affirm that the developed MHBN-APTES/Anti-T-Tau immunosensor exhibits commendable reproducibility across multiple tests. To further assess the reproducibility of the MHBN-APTES/Anti-T-Tau immunosensor, ten distinct immunosensors were fabricated, and DPV measurements were executed in the presence of 20 pg/mL T-Tau (Fig. 7B). The computed %cv and SD values were determined to be 3.21 % and ± 1.02, respectively. A %cv value of less than 5 % signifies high sensitivity for the developed immunosensor, indicating that there are minimal variances among the immunosensor groups and within the immunosensors themselves [71,92]. Stability studies were conducted to assess the response of the MHBN-APTES/Anti-T-Tau immunosensor over time when stored in a humidified environment at 4 °C for five days. The MHBN-APTES/Anti-T-Tau immunosensors were prepared, and DPV measurements were conducted daily to evaluate stability. After five days, the current response of the MHBN-APTES/Anti-T-Tau immunosensor exhibited only a 1.01 % decrease compared to the initial response (Fig. 7C). This result indicates that the immobilized Anti-T-Tau demonstrates significant stability over

the five days.

3.5. Sample application

Increased concentrations of T-Tau in blood serum are significantly associated with AD, making the detection of T-Tau essential. The commercial human serum (Sigma-Aldrich, H4522) were diluted 10 times with PBS (pH 7.4), and varying amounts of T-Tau (final concentrations 0.5, 20, and 50 pg/mL) were added to each dilution. The achieved recovery percentages with the diluted commercial human serum were given in Table 1. Given that acceptable recovery percentages range from 95 % to 105 %, this result affirms the system's validity [93,94].

The performance of biosensors designed for T-Tau detection in serum, as reported in the literature, was compared with the results of our study, as shown in Table 2. The findings underscore that the MHBN-APTES/Anti-T-Tau immunosensor possesses remarkable capabilities for detecting trace levels of T-Tau, exhibiting both high sensitivity and selectivity compared to the literature. The most widely used technique for detecting AD-related Tau pathology as a gold standard in the clinical field is Tau positron emission tomography (PET) molecular imaging [95,96]. However, commercial immunoassay kits for T-Tau levels in human serum exhibit linear detection ranges of 16 to 250000 pg/mL or 20 pg/mL to 1800 pg/mL. Given that the T-Tau concentration in the blood of individuals diagnosed with mild cognitive impairment is approximately 4.6 pg/mL, both of these immunoassay kits are only capable of identifying T-Tau in patient cohorts with advanced Alzheimer's disease. In this context, the MHBN-APTES/Anti-T-Tau immunosensor, which shows a linear determination range of 0.5–50 pg/mL, offers a potential that could be improved with further experiments such as real blood sample experiments for the early diagnosis of Alzheimer's disease and monitoring of disease progression.

Table 1
Detection of T-Tau in diluted human serum by the MHBN-APTES/Anti-T-Tau immunosensor (n = 3).

Sample	Added T-Tau (pg/mL)	Found T-Tau (pg/mL)	Recovery%
Human Serum	0.5	0.52 ± 0.19	104.00
	20	19.11 ± 1.32	95.55
	50	50.83 ± 0.77	101.66

Table 2
Comparison of the analytical performance of T-Tau immunosensors from serum.

	Modification	Linear Range	LOD	Reference
Electrochemical Immunosensors	PDDA nanolayer	10–10^5 pg/mL	1.31 pg/mL	[97]
	Tau/Anti-T-Tau/MPA	10^3–10^5 pg/mL	–	[98]
	HBN-PDA/Anti-T-Tau	1–30 pg/mL	0.42 pg/mL	[99]
	MHBN-APTES/Anti-T-Tau	0.5–50 pg/mL	0.39 pg/mL	**This work**

GO = Graphene oxide; pPG = poly (propyleneglycol), PLGA: poly (lactic-co-glycolic acid), AuNPs: Gold nanoparticles, PDDA: poly dimethyl diallyl ammonium chloride, PDA: polydopamine.

4. Conclusions

A novel electrochemical immunosensor based on MHBN-APTES has been developed as a label-free approach for detecting T-Tau in artificial blood serum. This immunosensor utilizes a modified SPCE integrating MHBN-APTES and Anti-T-Tau, characterized by a nanocomposite design incorporating a single biological molecule. The proposed MHBN-APTES/Anti-T-Tau immunosensor exhibited remarkable electrochemical performance for T-Tau detection, demonstrating a wide linear range between 0.5–50 pg/mL, high selectivity, and a LOD (0.39 pg/mL) at trace levels. Furthermore, the cost-effectiveness of the developed MHBN-APTES/Anti-T-Tau immunosensor renders it an attractive option for future enhancements and applications. It is also feasible to augment the capabilities of this immunosensing system to detect additional biomarkers related to neurodegenerative diseases, such as phospho-tau protein and amyloid beta (Aβ), by employing MHBN-APTES as a matrix for the immobilization of other antibodies. This progress could further broaden the scope of the immunosensors in early diagnostics and personalized medicine for neurodegenerative conditions. Although the developed MHBN-APTES/Anti-T-Tau immunosensor was designed for single use, this study's findings indicate that it has significant potential for rapid and minimally invasive detection of T-Tau, a biomarker associated with Alzheimer's disease.

CRediT authorship contribution statement

Simge Er Zeybekler: Writing – original draft, Methodology, Funding acquisition, Data curation, Conceptualization. **Dilek Odaci:** Writing – review & editing, Conceptualization. **Nesrin Horzum:** Writing – review & editing, Supervision, Funding acquisition, Conceptualization.

Declaration of competing interest

The authors declare that they have no known competing financial interests or personal relationships that could have appeared to influence the work reported in this paper.

Acknowledgements

S. Er Zeybekler and N. Horzum acknowledge the Scientific and Technological Research Council of Türkiye (TÜBİTAK) for financial support under the "2218 - National Postdoctoral Research Fellowship Program" (Project Number: 122C051).

Appendix A. Supplementary data

Supplementary data to this article can be found online at https://doi.org/10.1016/j.microc.2025.112811.

Data availability

Data will be made available on request.

References

[1] K.B. Magalingam, A. Radhakrishnan, N.S. Ping, N. Haleagrahara, Current concepts of neurodegenerative mechanisms in Alzheimer's disease, Biomed Res. Int. 2018 (2018) 3740461, https://doi.org/10.1155/2018/3740461.
[2] C. Di Natale, S. Russo, F. Graziano, V. Vespini, G. Luciani, G. Vitiello, L. Lombardi, F. Ferranti, S. Mari, P. Luca Maffettone, S. Grilli, S. Coppola, P. Ferraro, Sensitive colorimetric immunosensor using AuNP-functionalized polymer film for picogram-level detection of Tau protein intermediate aggregates, J. Colloid Interface Sci. 678 (2025) 1052–1059, https://doi.org/10.1016/j.jcis.2024.08.201.
[3] E. Nam, Y.B. Lee, C. Moon, K.A. Chang, Serum tau proteins as potential biomarkers for the assessment of Alzheimer's disease progression, Int. J. Mol. Sci. 21 (2020) doi: 10.3390%2Fijms21145007.
[4] T. Cheng, K. Jiao, M. Sun, J. Yu, J. Jiao, J. Jiao, Internal-driven DNA nanowindmill: Multi-fulcrum mediated amplified rolling nanomachine for fast and ultrasensitive electrochemical detection of tau, Sens. Actuators B 423 (2025) 136797, https://doi.org/10.1016/j.snb.2024.136797.
[5] M. Adampourezare, M. Hasanzadeh, B. Nikzad, Recent progress and challenges in the application of molecularly imprinted polymers for early-stage screening of neurodegenerative diseases-related protein biomarkers, Microchem. J. 192 (2023) 108931, https://doi.org/10.1016/j.microc.2023.108931.
[6] C. Laske, H.R. Sohrabi, S.M. Frost, K. López-de-Ipiña, P. Garrard, M. Buscema, J. Dauwels, S.R. Soekadar, S. Mueller, C. Linnemann, Innovative diagnostic tools for early detection of Alzheimer's disease, A&D 11 (2015) 561–578, https://doi.org/10.1016/j.jalz.2014.06.004.
[7] C.-C. Yang, M.-J. Chiu, T.-F. Chen, H.-L. Chang, B.-H. Liu, S.-Y. Yang, Assay of plasma phosphorylated tau protein (threonine 181) and total tau protein in early-

stage Alzheimer's disease, Am. J. Alzheimer's Dis. 61 (2018) 1323–1332, https://doi.org/10.3233/JAD-170810.
[8] L.-F. Lue, M.N. Sabbagh, M.-J. Chiu, N. Jing, N.L. Snyder, C. Schmitz, A. Guerra, C. M. Belden, T.-F. Chen, C.-C. Yang, Plasma levels of Aβ42 and tau identified probable Alzheimer's dementia: findings in two cohorts, Front. Aging Neurosci. 9 (2017) 226, doi: 10.3389%2Ffnagi.2017.00226.
[9] Y. Liu, H. Qing, Y. Deng, Biomarkers in Alzheimer's disease analysis by mass spectrometry-based proteomics, Int. J. Mol. Sci. 15 (2014) 7865–7882, https://doi.org/10.3390/ijms15057865.
[10] I. Hossain, M. Mohammadian, R.S. Takala, O. Tenovuo, L. Lagerstedt, H. Ala-Seppälä, J. Frantzén, M. Van Gils, P. Hutchinson, A.J. Katila, Early levels of glial fibrillary acidic protein and neurofilament light protein in predicting the outcome of mild traumatic brain injury, J. Neurotrauma 36 (2019) 1551–1560, https://doi.org/10.1089/neu.2018.5952.
[11] R. Bruch, J. Baaske, C. Chatelle, M. Meirich, S. Madlener, W. Weber, C. Dincer, G. A. Urban, CRISPR/Cas13a-powered electrochemical microfluidic biosensor for nucleic acid amplification-free miRNA diagnostics, Adv. Mater. 31 (2019) 1905311, https://doi.org/10.1002/adma.201905311.
[12] S. Khetani, R. Aburashed, A. Singh, A. Sen, A. Sanati-Nezhad, Immunosensing of S100β biomarker for diagnosis of spinal cord injuries (SCI), Sens. Actuat. B-Chem. 247 (2017) 163–169, https://doi.org/10.1016/j.snb.2017.02.169.
[13] H. Ma, Y. Xing, B. Cui, J. Han, B. Wang, Z. Zeng, Recent advances in two-dimensional layered and non-layered materials hybrid heterostructures, Chin. Phys. B (2022), https://doi.org/10.1088/1674-1056/ac5c36.
[14] A. Sanati, Y. Esmaeili, E. Bidram, L. Shariati, M. Rafienia, S. Mahshid, O. Parlak, Recent advancement in electrode materials and fabrication, microfluidic designs, and self-powered systems for wearable non-invasive electrochemical glucose monitoring, Appl. Mater. Today 26 (2022) 101350, https://doi.org/10.1016/j.apmt.2021.101350.
[15] A.C. Sparavigna, Iron Oxide Fe3O4 Nanoparticles for Electromagnetic Shielding, (2023). doi: 10.26434/chemrxiv-2023-g9bkz-v2.
[16] D.M.A. Neto, L.S. da Costa, C.P. Sousa, H. Becker, P.N.S. Casciano, H. O. Nascimento, J.R.B. Neto, P. de Lima-Neto, R.F. Nascimento, J.A.C. Guedes, R. C. de Oliveira, D. Zampieri, A.N. Correia, P.B.A. Fechine, Functionalized Fe3O4 nanoparticles for electrochemical sensing of carbendazim, Electrochim. Acta 432 (2022) 141193, https://doi.org/10.1016/j.electacta.2022.141193.
[17] F. Mollarasouli, E. Zor, G. Ozcelikay, S.A. Ozkan, Magnetic nanoparticles in developing electrochemical sensors for pharmaceutical and biomedical applications, Talanta 226 (2021) 122108, https://doi.org/10.1016/j.talanta.2021.122108.
[18] F.G. Nejad, S. Tajik, H. Beitollahi, I. Sheikhshoaie, Magnetic nanomaterials based electrochemical (bio) sensors for food analysis, Talanta 228 (2021) 122075, https://doi.org/10.1016/j.talanta.2020.122075.
[19] G. Sridharan, C.J.T. Godwin, R. Atchudan, S. Arya, M. Govindasamy, S.M. Osman, A.K. Sundramoorthy, Iron oxide decorated hexagonal boron nitride modified electrochemical sensor for the detection of nitrofurantoin in human urine samples, J. Taiwan Inst. Chem. Eng. 163 (2024) 105320, https://doi.org/10.1016/j.jtice.2023.105320.
[20] D. Park, J.H. Kim, H.J. Kim, D. Lee, D.S. Lee, D.S. Yoon, K.S. Hwang, Multiplexed femtomolar detection of Alzheimer's disease biomarkers in biofluids using a reduced graphene oxide field-effect transistor, Biosens. Bioelectron. 167 (2020) 112505, https://doi.org/10.1016/j.bios.2020.112505.
[21] B.B. Yola, C. Karaman, N. Özcan, N. Atar, İ. Polat, M.L. Yola, Electrochemical tau protein immunosensor based on MnS/GO/PANI and magnetite-incorporated gold nanoparticles, Electroanalysis 34 (2022) 1519–1528, https://doi.org/10.1002/elan.202200159.
[22] Y. Liu, X. Liu, M. Li, Q. Liu, T. Xu, Portable vertical graphene@ Au-based electrochemical aptasensing platform for point-of-care testing of Tau protein in the blood, Biosensors 12 (2022) 564, https://doi.org/10.3390/bios12080564.
[23] M.N.S. Karaboga, M.K. Sezgintürk, Analysis of Tau-441 protein in clinical samples using rGO/AuNP nanocomposite-supported disposable impedimetric neuro-biosensing platform: Towards Alzheimer's disease detection, Talanta 219 (2020) 121257, https://doi.org/10.1016/j.bios.2016.10.019.
[24] Y. Zhang, Y.-N. Wang, X.-T. Sun, L. Chen, Z.-R. Xu, Boron nitride nanosheet/CuS nanocomposites as mimetic peroxidase for sensitive colorimetric detection of cholesterol, Sens. Actuators B Chem. 246 (2017) 118–126, https://doi.org/10.1016/j.snb.2017.02.059.
[25] S. Ketmen, S. Er Zeybekler, S.S. Gelen, D. Odaci, Graphene oxide-magnetic nanoparticles loaded polystyrene-polydopamine electrospun nanofibers based nanocomposites for immunosensing application of C-reactive protein, Biosensors 12 (2022) 1175, https://doi.org/10.3390/bios12121175.
[26] R.S. Bangari, V.K. Yadav, J.K. Singh, N. Sinha, Fe3O4-functionalized boron nitride nanosheets as novel adsorbents for removal of arsenic(III) from contaminated water, ACS Omega 5 (2020) 10301–10314, https://doi.org/10.1021/acsomega.9b04295.
[27] S. Emami, M.M. Alavi Nikje, Recyclable nanomagnetic Fe3O4@ APTES catalyst role on the hydrolysis of polycarbonate wastes, Mex. Chem. Soc. 62 (2018) 204–213, https://doi.org/10.29356/jmcs.v62i4.651.
[28] S. Hemmati, M.M. Heravi, B. Karmakar, H. Veisi, In situ decoration of Au NPs over polydopamine encapsulated GO/Fe3O4 nanoparticles as a recyclable nanocatalyst for the reduction of nitroarenes, Sci. Rep. 11 (2021) 12362, https://doi.org/10.1038/s41598-021-90514-x.
[29] S.F. Chin, K.S. Iyer, C.L. Raston, Fabrication of carbon nano-tubes decorated with ultra fine superparamagnetic nano-particles under continuous flow conditions, Lab Chip 8 (2008) 439–442, https://doi.org/10.1039/B716195F.
[30] D.Ç. Varan, Development of amino functionalized POSS based (3-Glycidoxypropyl) trimethoxysilane hybrid sol-gel coatings for aircraft applications, Middle East Technical University (2021).
[31] S. Er, D.O. Demirkol, Graphene oxide incorporated polystyrene electrospun nanofibers for immunosensing of CD36 as a marker of diabetic plasma, Bioelectrochemistry 145 (2022) 108083, https://doi.org/10.1016/j.bioelechem.2022.108083.
[32] P. Rana, R. Dixit, S. Sharma, S. Dutta, S. Yadav, B. Arora, B. Priyanka, M. B. Kaushik, R.K.S. Gawande, Insights into the catalytic potential of a rationally designed magnetic boron nitride nanosheet supported nickel catalyst for the efficient synthesis of 1,4-dihydropyridines, React. Chem. Eng. 8 (2023) 244–253, https://doi.org/10.1039/D2RE00246A.
[33] C. Zhang, Y. He, F. Li, H. Di, L. Zhang, Y. Zhan, h-BN decorated with Fe3O4 nanoparticles through mussel-inspired chemistry of dopamine for reinforcing anticorrosion performance of epoxy coatings, J. Alloy. Compd. 685 (2016) 743–751, https://doi.org/10.1016/j.jallcom.2016.06.220.
[34] M.F. Khalid, I. Riaz, R. Jalil, U. Mahmood, R.R. Mir, H.A. Sohail, Dielectric properties of multi-layers hexagonal boron nitride, MSA 11 (2020) 339–346.
[35] P. Thangasamy, M. Sathish, Supercritical fluid processing: a rapid, one-pot exfoliation process for the production of surfactant-free hexagonal boron nitride nanosheets, CrstEngComm 17 (2015) 5895–5899, https://doi.org/10.1039/C5CE00926J.
[36] T. Wang, M. Wang, L. Fu, Z. Duan, Y. Chen, X. Hou, Y. Wu, S. Li, L. Guo, R. Kang, Enhanced thermal conductivity of polyimide composites with boron nitride nanosheets, Sci. Rep. 8 (2018) 1557, https://doi.org/10.1038/s41598-018-19945-3.
[37] R.S. Bangari, V.K. Yadav, J.K. Singh, N. Sinha, Fe3O4-Functionalized boron nitride nanosheets as novel adsorbents for removal of arsenic (III) from contaminated water, ACS Omega 5 (2020) 10301–10314.
[38] P. Rana, R. Dixit, S. Sharma, S. Dutta, S. Yadav, B. Arora, B. Kaushik, P. Rana, R. K. Sharma, Magnetic boron nitride nanosheets decorated with cobalt nanoparticles as catalyst for the synthesis of 3, 4-dihydropyrimidin-2 (1H)-ones/thiones, ACS Appl. Nano Mater. 5 (2022) 4875–4886, https://doi.org/10.1021/acsanm.1c04438.
[39] C. Xu, Y. Su, D. Liu, X. He, Three-dimensional N, B-doped graphene aerogel as a synergistically enhanced metal-free catalyst for the oxygen reduction reaction, PCCP 17 (2015) 25440–25448, https://doi.org/10.1039/C5CP04211A.
[40] Q. Xue, H. Zhang, M. Zhu, Z. Wang, Z. Pei, Y. Huang, Y. Huang, X. Song, H. Zeng, C. Zhi, Hydrothermal synthesis of blue-fluorescent monolayer BN and BCNO quantum dots for bio-imaging probes, RSC Adv. 6 (2016) 79090–79094, https://doi.org/10.1039/C6RA16744F.
[41] P.K. Rastogi, K.R. Sahoo, P. Thakur, R. Sharma, S. Bawari, R. Podila, T. N. Narayanan, Graphene–hBN non-van der Waals vertical heterostructures for four-electron oxygen reduction reaction, PCCP 21 (2019) 3942–3953, https://doi.org/10.1039/C8CP06155F.
[42] Q. An, F. Lv, Q. Liu, C. Han, K. Zhao, J. Sheng, Q. Wei, M. Yan, L. Mai, Amorphous vanadium oxide matrixes supporting hierarchical porous Fe3O4/graphene nanowires as a high-rate lithium storage anode, Nano Lett. 14 (2014) 6250–6256, https://doi.org/10.1021/nl5025694.
[43] A.G. Nene, M. Takahashi, P.R. Somani, Fe 3 O 4 and Fe nanoparticles by chemical reduction of Fe (acac) 3 by ascorbic acid: role of water, WJNSE 6 (2016) 20, https://doi.org/10.4236/wjnse.2016.61002.
[44] Q. Ai, Z. Yuan, R. Huang, C. Yang, G. Jiang, J. Xiong, Z. Huang, S. Yuan, One-pot co-precipitation synthesis of Fe3O4 nanoparticles embedded in 3D carbonaceous matrix as anode for lithium ion batteries, J. Mater. Sci. 54 (2019) 4212–4224, https://doi.org/10.1007/s10853-018-3141-3.
[45] G.-I. Lupu, C. Orbeci, C. Bobirică, L. Bobirică, E.S. Lazăr, J. Pandele-Cusu, M. N. Verziu, C. Pîrvu, R.-G. Irodia, Photocatalytic degradation of azithromycin formulation in aqueous solution by doped titanium dioxide/fiberglass-rubberized silicone photocatalytic membrane, Sustain. Environ. Res. 33 (2023) 36, https://doi.org/10.1186/s42834-023-00199-2.
[46] M. Manjunatha, R. Kumar, A.V. Anupama, V.B. Khopkar, R. Damle, K.P. Ramesh, B. Sahoo, XRD, internal field-NMR and Mössbauer spectroscopy study of composition, structure and magnetic properties of iron oxide phases in iron ores, JMR&T 8 (2019) 2192–2200, https://doi.org/10.1016/j.jmrt.2019.01.022.
[47] D. Zhang, X. Du, Y. Song, H. Sun, Y. Zheng, Z. Sun, Y. She, B. Wang, Oxidation mechanism and microstructure evolution of invar alloy with high temperature annealing process, JMR&T 32 (2024) 185–195, https://doi.org/10.1016/j.jmrt.2024.07.150.
[48] W. Wu, Q. He, H. Chen, J. Tang, L. Nie, Sonochemical synthesis, structure and magnetic properties of air-stable Fe3O4/Au nanoparticles, Nanotechnology 18 (2007) 145609, https://doi.org/10.1088/0957-4484/18/14/145609.
[49] M. Boksebeld, V. Kilin, A. Geloen, G. Ceccone, A. Jaffal, C. Schmidt, S. Alekseev, V. Lysenko, J.-P. Wolf, L. Bonacina, Folate-modified silicon carbide nanoparticles as multiphoton imaging nanoprobes for cancer-cell-specific labeling, RSC Adv. 7 (2017) 27361–27369, https://doi.org/10.1039/C7RA03961A.
[50] D.B. Knorr Jr, K.S. Williams, N.F. Baril, C. Weiland, J.W. Andzelm, J.L. Lenhart, J. C. Woicik, D.A. Fischer, M.Z. Tidrow, S.V. Bandara, Use of 3-aminopropyltriethoxysilane deposited from aqueous solution for surface modification of III-V materials, Appl. Surf. Sci. 320 (2014) 414–428, https://doi.org/10.1016/j.apsusc.2014.09.055.
[51] M. Maaz, T. Elzein, D. Dragoe, A. Bejjani, N. Jarroux, C. Poulard, N. Aubry-Barroca, B. Nsouli, P. Roger, Poly (4-vinylpyridine)-modified silica for efficient oil/water separation, J. Mater. Sci. 54 (2019) 1184–1196, https://doi.org/10.1007/s10853-018-2888-x.

[52] I.S. Merenkov, M.S. Myshenkov, Y.M. Zhukov, Y. Sato, T.S. Frolova, D.V. Danilov, I.A. Kasatkin, O.S. Medvedev, R.V. Pushkarev, O.I. Sinitsyna, M. Terauchi, I. A. Zvereva, M.L. Kosinova, K. Ostrikov, Orientation-controlled, low-temperature plasma growth and applications of h-BN nanosheets, Nano Res. 12 (2019) 91–99, https://doi.org/10.1007/s12274-018-2185-7.
[53] V. Karade, A. Sharma, R. Dhavale, R. Dhavale, S. Shingte, P. Patil, J. Kim, D. Zahn, A. Chougale, G. Salvan, APTES monolayer coverage on self-assembled magnetic nanospheres for controlled release of anticancer drug Nintedanib, Sci. Rep. 11 (2021) 5674, https://doi.org/10.1038/s41598-021-84770-0.
[54] Y. Liu, S. Zhang, Y. He, C. Chen, C. Zhang, P. Xie, F. Zhong, H. Li, J. Chen, Z. Li, APTES modification of molybdenum disulfide to improve the corrosion resistance of waterborne epoxy coating, Coatings 11 (2021) 178, https://doi.org/10.3390/coatings11020178.
[55] R.S. Alruwais, W.A. Adeosun, H.M. Marwani, M. Jawaid, A.M. Asiri, A. Khan, Novel aminosilane (APTES)-grafted polyaniline@ graphene oxide (PANI-GO) nanocomposite for electrochemical sensor, Polymers 13 (2021) 2562, https://doi.org/10.3390/polym13152562.
[56] M. Tong, J. Cao, X. Chen, H. Zhang, W. Wu, H. Ma, Self-assembly of chemically modified graphene sheets in an external magnetic field, RSC Adv. 9 (2019) 19457–19464, https://doi.org/10.1039/C9RA01807G.
[57] C. Tsukada, S. Ogawa, H. Niwa, T. Nomoto, G. Kutluk, H. Namatame, M. Taniguchi, S. Yagi, Morphological and spectroscopic studies on enlargement of Pd nanoparticle in l-cysteine aqueous solution by AFM and XPS, Appl. Surf. Sci. 267 (2013) 48–52, https://doi.org/10.1016/j.apsusc.2012.05.123.
[58] A. Miranda, L. Martínez, P.A.A. De Beule, Facile synthesis of an aminopropylsilane layer on Si/SiO2 substrates using ethanol as APTES solvent, MethodsX 7 (2020) 100931, https://doi.org/10.1016/j.mex.2020.100931.
[59] A. Sultan, F. Mohammad, Chemical sensing, thermal stability, electrochemistry and electrical conductivity of silver nanoparticles decorated and polypyrrole enwrapped boron nitride nanocomposite, Polymer 113 (2017) 221–232, https://doi.org/10.1016/j.polymer.2017.02.074.
[60] Y. Zhang, Y. Cheng, Y. Zhou, B. Li, W. Gu, X. Shi, Y. Xian, Electrochemical sensor for bisphenol A based on magnetic nanoparticles decorated reduced graphene oxide, Talanta 107 (2013) 211–218, https://doi.org/10.1016/j.talanta.2013.01.012.
[61] P. Ananthappan, M. Thangarasu, V. Sivasamy Vasantha, Effect of electrophoretic deposition for selective detection of Pb2+ ions using nitrogen and sulphur-doped reduced graphene oxide, Microchem. J. 203 (2024) 110879, https://doi.org/10.1016/j.microc.2024.110879.
[62] J. Wang, H. Ouyang, Y. Ni, H. Zhang, L. Sun, R. Liu, S. Li, Magnetic self-assembled label-free electrochemical biosensor based on Fe3O4/α-Fe2O3 heterogeneous nanosheets for the detection of Tau proteins, Bioelectrochemistry 157 (2024) 108678, https://doi.org/10.1016/j.bioelechem.2024.108678.
[63] M. Shahabuddin, A.K. Wilson, A.C. Koech, N. Noginova, Probing charge transport kinetics in a plasmonic environment with cyclic voltammetry, ACS Omega 6 (2021) 34294–34300, https://doi.org/10.1021/acsomega.1c03794.
[64] A. Farida, E. Fitriany, A. Baktir, F. Kurniawan, M. Harsini, Voltammetric study of ascorbic acid using polymelamine/gold nanoparticle modified carbon paste electrode, IOP Conf. Series: Earth Environ. Sci., IOP Publishing (2019) 012004, https://doi.org/10.1088/1755-1315/217/1/012004.
[65] M. Mohammad Hossein, M. Amoli-Diva, Drug-carrying amino silane coated magnetic nanoparticles as potential vehicles for delivery of antibiotics, J. Nanomed. Nanotechnol. (2012), https://doi.org/10.4172/2157-7439.1000139.
[66] U. Mengulluoglu, B.A. Guler, S.E. Zeybekler, E. Imamoglu, D. Odaci, Enzymes on chemical gardens: Chemobrionics-based electrochemical biosensor, Microchem. J. 205 (2024) 111192, https://doi.org/10.1016/j.microc.2024.111192.
[67] S. Er Zeybekler, D. Odaci, Carbon nanotube-incorporated nanofibers for immunosensor preparation against CD36, ACS Omega 8 (2023) 5776-5786. doi: 10.1021/acsomega.2c07458.
[68] J. Zhou, H.-K. Tsao, Y.-J. Sheng, S. Jiang, Monte Carlo simulations of antibody adsorption and orientation on charged surfaces, J. Chem. Phys. 121 (2004) 1050–1057, https://doi.org/10.1021/la026871z.
[69] B.J. Polk, A. Stelzenmuller, G. Mijares, W. MacCrehan, M. Gaitan, Ag/AgCl microelectrodes with improved stability for microfluidics, Sens. Actuators B: Chem. 114 (2006) 239–247, https://doi.org/10.1016/j.snb.2005.03.121.
[70] A.H. Talasaz, M. Nemat-Gorgani, Y. Liu, P. Ståhl, R.W. Dutton, M. Ronaghi, R. W. Davis, Prediction of protein orientation upon immobilization on biological and nonbiological surfaces, PNAS 103 (2006) 14773–14778, https://doi.org/10.1073/pnas.0605841103.
[71] D.A. Skoog, F.J. Holler, S.R. Crouch, Principles of instrumental analysis, Cengage Learning (2017).
[72] A.C. Lazanas, M.I. Prodromidis, Electrochemical impedance spectroscopy—A tutorial, ACS Meas. Sci. Au 3 (2023) 162–193, https://doi.org/10.1021/acsmeasuresciau.2c00070.
[73] R.P. Talemi, S.M. Mousavi, H. Afruzi, Using gold nanostars modified pencil graphite electrode as a novel substrate for design a sensitive and selective Dopamine aptasensor, Mater. Sci. Eng. C 73 (2017) 700–708, https://doi.org/10.1016/j.msec.2016.12.119.
[74] M.H.M. Zaid, J. Abdullah, N.A. Yusof, H. Wasoh, Y. Sulaiman, M.F.M. Noh, R. Issa, Reduced graphene oxide/TEMPO-nanocellulose nanohybrid-based electrochemical biosensor for the determination of mycobacterium tuberculosis, J. Sens. 2020 (2020) 4051474, https://doi.org/10.1155/2020/4051474.
[75] P. Assari, A.A. Rafati, A. Feizollahi, R. Asadpour Joghani, An electrochemical immunosensor for the prostate specific antigen based on the use of reduced graphene oxide decorated with gold nanoparticles, Mikrochim. Acta 186 (2019) 484, https://doi.org/10.1007/s00604-019-3565-8.
[76] P. Yadav, S. Manivannan, H.S. Kim, K. Pandey, K. Kim, J. Kim, Electrochemical properties of highly sensitive and selective CuO nanostructures based neurotransmitter dopamine sensor, Electroanalysis 29 (2017) 2106–2113, https://doi.org/10.1002/elan.201700195.
[77] P. Ranjan, M. Abubakar Sadique, S. Yadav, R. Khan, An electrochemical immunosensor based on gold-graphene oxide nanocomposites with ionic liquid for detecting the breast cancer CD44 biomarker, ACS Appl. Mater. Interfaces 14 (2022) 20802–20812, https://doi.org/10.1021/acsami.2c03905.
[78] Y. Liu, T. Wu, H. Zhao, G. Zhu, F. Li, M. Guo, Q. Ran, S. Komarneni, An electrochemical sensor modified with novel nanohybrid of Super-P carbon black@ zeolitic-imidazolate-framework-8 for sensitive detection of carbendazim, Ceram. Int. 49 (2023) 23775–23787, https://doi.org/10.1016/j.ceramint.2023.04.217.
[79] S. Er, D. Odaci Demirkol, Graphene oxide incorporated polystyrene electrospun nanofibers for immunosensing of CD36 as a marker of diabetic plasma, Bioelectrochemistry 145 (2022) 108083, https://doi.org/10.1016/j.bioelechem.2022.108083.
[80] X. Ding, S. Zhang, L. Jiang, L. Wang, T. Li, P. Lei, Ultrasensitive assays for detection of plasma tau and phosphorylated tau 181 in Alzheimer's disease: a systematic review and meta-analysis, Transl. Neurodegener. 10 (2021) 1–14, https://doi.org/10.1186/s40035-021-00234-5.
[81] J.L. Dage, A.M. Wennberg, D.C. Airey, C.E. Hagen, D.S. Knopman, M.M. Machulda, R.O. Roberts, C.R. Jack Jr, R.C. Petersen, M.M. Mielke, Levels of tau protein in plasma are associated with neurodegeneration and cognitive function in a population-based elderly cohort, Alzheimers Dement. 12 (2016) 1226–1234, https://doi.org/10.1016/j.jalz.2016.06.001.
[82] S.K. Vashist, J.H. Luong, Bioanalytical requirements and regulatory guidelines for immunoassays, in: Handbook of Immunoassay Technologies, Elsevier, 2018, pp. 81–95.
[83] M. Maiga, E.E. Yalcinkaya, B. Sonmez, D. Puglia, M. Yavuz, D.O. Demirkol, J. M. Kenny, S. Timur, CTAB modified dellite: A novel support for enzyme immobilization in bio-based electrochemical detection and its in vitro antimicrobial activity, Sens. Actuators B: Chem. 235 (2016) 46–55, https://doi.org/10.1016/j.snb.2016.05.042.
[84] A. Govind Rajan, M.S. Strano, D. Blankschtein, Liquids with lower wettability can exhibit higher friction on hexagonal boron nitride: the intriguing role of solid–liquid electrostatic interactions, Nano Lett. 19 (2019) 1539–1551, https://doi.org/10.1021/acs.nanolett.8b04335.
[85] O. Neděla, P. Slepička, V. Švorčík, Surface modification of polymer substrates for biomedical applications, Materials 10 (2017) 1115, https://doi.org/10.3390/ma10101115.
[86] H. Teymourian, A. Salimi, S. Khezrian, Fe3O4 magnetic nanoparticles/reduced graphene oxide nanosheets as a novel electrochemical and bioeletrochemical sensing platform, Biosens. Bioelectron. 49 (2013) 1–8, https://doi.org/10.1016/j.bios.2013.04.034.
[87] A. Sheinenzon, M. Shehadeh, R. Michelis, E. Shaoul, O. Ronen, Serum albumin levels and inflammation, Int. J. Biol. Macromol. 184 (2021) 857–862, https://doi.org/10.1016/j.ijbiomac.2021.06.140.
[88] G. Baura, Medical Device Technologies: A Systems Based Overview Using Engineering Standards, Academic Press, 2011.
[89] E. Carmina, F.Z. Stanczyk, R.A. Lobo, Chapter 34 - Evaluation of hormonal status, in: J.F. Strauss, R.L. Barbieri (Eds.), Yen and Jaffe's Reproductive Endocrinology (eighth Edition), Elsevier, Philadelphia, 2019, pp. 887–915.e884, https://doi.org/10.1016/B978-0-323-47912-7.00034-2.
[90] S.M. Bagshaw, R. Bellomo, Kidney-Lung Interactions, Mechanical Ventilation E-Book: Clinical Applications and Pathophysiology (2007) 195.
[91] A. Kamal, Estimation of blood urea (BUN) and serum creatinine level in patients of renal disorder, Indian J. Fundam. Appl. Life Sci. 4 (2014) 199–202.
[92] A. Oner, E. Tufek, I. Yezer, A. Birol, M. Demir, S. Er, D.O. Demirkol, High generation dendrimer decorated poly-Ɛ-caprolactone/polyacrylic acid electrospun nanofibers for the design of a bioelectrochemical sensing surface, React. Funct. Polym. 161 (2021) 104853, https://doi.org/10.1016/j.reactfunctpolym.2021.104853.
[93] K.-F. Peng, H.-W. Zhao, X.-F. Wu, Signal-enhanced electrochemical immunosensor for CD36 based on cascade catalysis of a GOx labeled Prussian blue functionalized Ceria nanohybrid, RSC Adv. 5 (2015) 1812–1817, https://doi.org/10.1039/C4RA10413G.
[94] I. Taverniers, M. De Loose, E. Van Bockstaele, Trends in quality in the analytical laboratory. II. Analytical method validation and quality assurance, Trends Analyt. Chem. 23 (2004) 535–552, https://doi.org/10.1016/j.trac.2004.04.001.
[95] G. Cassinelli Petersen, M. Roytman, G.C. Chiang, Y. Li, M.L. Gordon, A. M. Franceschi, Overview of tau PET molecular imaging, Curr. Opin. Neurol. 35 (2022) 230–239, https://doi.org/10.1097/wco.0000000000001035.
[96] G.N. Bischof, A. Dodich, M. Boccardi, T. van Eimeren, C. Festari, H. Barthel, O. Hansson, A. Nordberg, R. Ossenkoppele, O. Sabri, B.F.G. Giovanni, V. Garibotto, A. Drzezga, Clinical validity of second-generation tau PET tracers as biomarkers for Alzheimer's disease in the context of a structured 5-phase development framework, Eur. J. Nucl. Med. Mol. Imaging 48 (2021) 2110–2120, https://doi.org/10.1007/s00259-020-05156-4.
[97] Q. Chen, J. Hu, Z. Mao, K. Koh, H. Chen, Loach mucus-like guanosine-based hydrogel as an antifouling coating for electrochemical detection of tau protein,

Sens. Actuators B: Chem. 370 (2022) 132419, https://doi.org/10.1016/j.snb.2022.132419.

[98] Y. Dai, A. Molazemhosseini, C.C. Liu, A. Single-Use, In vitro biosensor for the detection of T-tau protein, a biomarker of neuro-degenerative disorders, in PBS and human serum using differential pulse voltammetry (DPV), Biosensors 7 (2017) 10, https://doi.org/10.3390/bios7010010.

[99] S. Er Zeybekler, Polydopamine-coated hexagonal boron nitride-based electrochemical immunosensing of T-Tau as a marker of Alzheimer's disease, Bioelectrochemistry 154 (2023) 108552, https://doi.org/10.1016/j.bioelechem.2023.108552.